SECTION 1

RESEARCH IN PROGRESS

NUCLEAR REACTIONS -- EXPERIMENTAL

CROSS COMPARISONS OF NUCLEAR TEMPERATURES DETERMINED FROM EXCITED STATES POPULATIONS AND ISOTOPE YIELDS

M.B. Tsang, F. Zhu[a] , W.G. Lynch, A. Aranda[b] , D.R. Bowman[c] , R.T. de Souza[d] , C.K. Gelbke, Y.D. Kim[e] , L. Phair[f] , S. Pratt, C. Williams, and H.M. Xu[g] and W.A. Friedman[h]

Recently, nuclear temperatures have been extracted from the relative yields of Li and He isotopes [1], assuming chemical and thermal equilibrium at freeze-out [2] and using the expression [1,2]:

$$T = \frac{B}{ln(a \bullet R)} \tag{1}$$

Here, R denotes the measured ratio of isotopic yields, B is a binding energy parameter and a depends on the nuclear spins. The latter two parameters were calculated by assuming that the relative yields of nucleus of charge Z_i and A_i are given by the corresponding ground state yields of these nuclei under the assumption of thermal equilibrium. In the approximate expression utilized by refs. [1, 2],

$$R = \frac{Y(A_i, Z_i)/Y(A_i + 1, Z_i)}{Y(A_j, Z_j)/Y(A_j + 1, Z_j)} \tag{2}$$

$$B = BE(A_i, Z_i) - BE(A_i + 1, Z_i) - BE(A_j, Z_j) + BE(A_j + 1, Z_j) \tag{3}$$

$$a = \frac{(2S(A_j, Z_j) + 1)/(2S(A_j + 1, Z_j) + 1)}{(2S(A_i, Z_i) + 1)/(2S(A_i + 1, Z_i) + 1)} \bullet \left[\frac{A_j/(A_j + 1)}{A_i/(A_i + 1)}\right]^{\eta} \tag{4}$$

where $Y(A_i, Z_i)$, $BE(A_i, Z_i)$ and $S(A_i, Z_i)$ are the measured total yield, and the known binding energy and spin of the ground state of a specific isotope with mass A_i and charge Z_i. The exponent η arises from an integration over the energy spectrum and equals 1.5 in the limit of volume emission, and 1.0 in the limit of surface emission.

The temperature measurements performed for ^{197}Au+^{197}Au collisions at an incident energy of 600 AMeV as a function of the deduced excitation energy deposited in the projectile-like residue [1] are shown in the left panel of Fig. 1. This observation of a "caloric" curve characterized by a plateau followed by a rise in temperature qualitatively reproduces many of the essential predictions of Microcanonical models [3,4].

In the past, thermometers based upon the relative populations of excited states of emitted light nuclei have the advantage that they are insensitive to collective motion [5-10]. Such thermometers have been cross calibrated by measuring the decay of hot compound nuclei [11] and have been employed in investigations over a wide range of bombarding energies [5-10]. Temperatures extracted from the relative yields of isotopes can be strongly influenced by the fact that Coulomb and collective energies are mass dependent [12,13] while the thermal energy is not. The energy spectra of different isotopes may display different slopes. Such effects do not influence temperatures extracted from the relative populations of excited states. Since the sensitivities of the two techniques to the sequential decay of heavier particle unstable nuclei that feed the measured yields are different, a cross calibration of the two techniques is

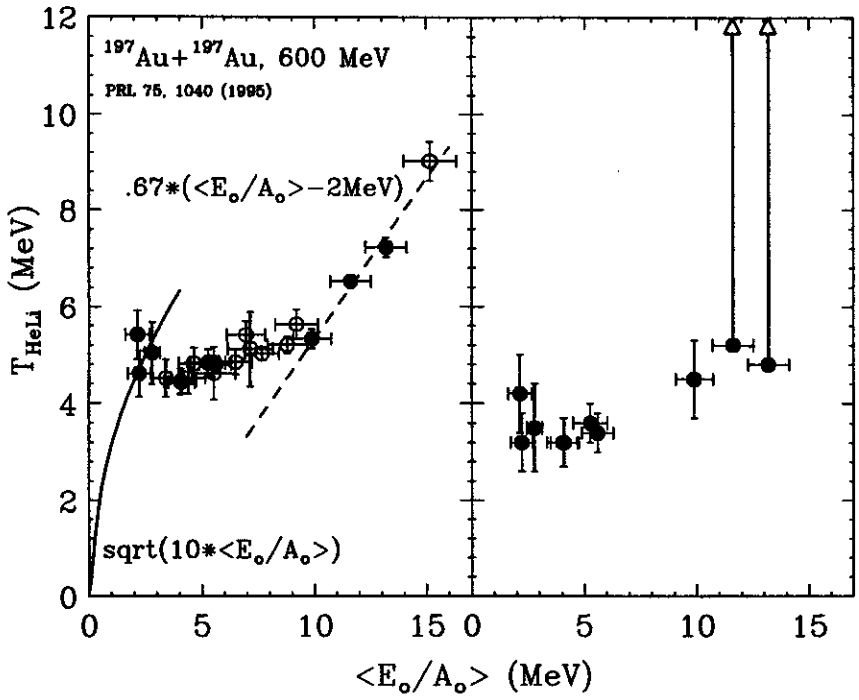

Figure 1: Left panel: Relationship between T_{LiHe} and $< E_o/A_o >$ for $Au + Au$ collisions at $E/A = 600$ MeV from ref. 1. The solid points are the ones analyzed in this work. Right panel : Corresponding values for T_{em} extracted after detailed corrections for secondary decay.

relevant. For this purpose, we extract isotope temperatures for the ^{36}Ar+^{197}Au reaction at 35 AMeV and compare them to temperatures extracted from excited states populations measured for the same experiment [14,15].

The experiment was performed at the National Superconducting Cyclotron Laboratory at Michigan State University. Beams of ^{36}Ar ions at 35A MeV from the NSCL K500 cyclotron bombarded ^{197}Au targets of 1 mg/cm^2 areal density in the 92" scattering chamber. Isotopes from Z=1 to Z=5 were measured with an array of 13 closely packed position sensitive gas-ΔE-E telescopes. Four of the telescopes located at θ_{lab} = 33.7° and 45.1° were optimized to detect charge particles with Z>2 (HF) and the remaining telescopes were optimized to measure light charge particles. As the present ratios involve Lithium fragments, data detected with the HF telescopes will be primarily used. Each HF telescope subtended a solid angle of 5.6 msr and consisted of 75 μm and 100 μm thick surface-barrier silicon ΔE detectors and a 5 mm lithium-drifted Si(Li) E detector.

In addition to the hodoscope, the associated charge particle mulitiplicityy was measured with the MSU Miniball [15,16] which cover 77% of 4π. Data from the combined array were analyzed in refs. [14,15] to study the impact parameter dependence of temperatures extracted from the excited state populations. Futher details about the experimental set up and the algorithms used in defining central collision events are given in ref. [15]. Examination of the excited states popuplation for this reaction revealed that the populations were more consistent with thermal equilibrium for central collisions with reduced impact parameter $\hat{b}$=b/b_{max} $\leq$ 0.3 than for peripheral collisions with $\hat{b}\geq$0.6 [15]; b_{max} corresponds to the maximum

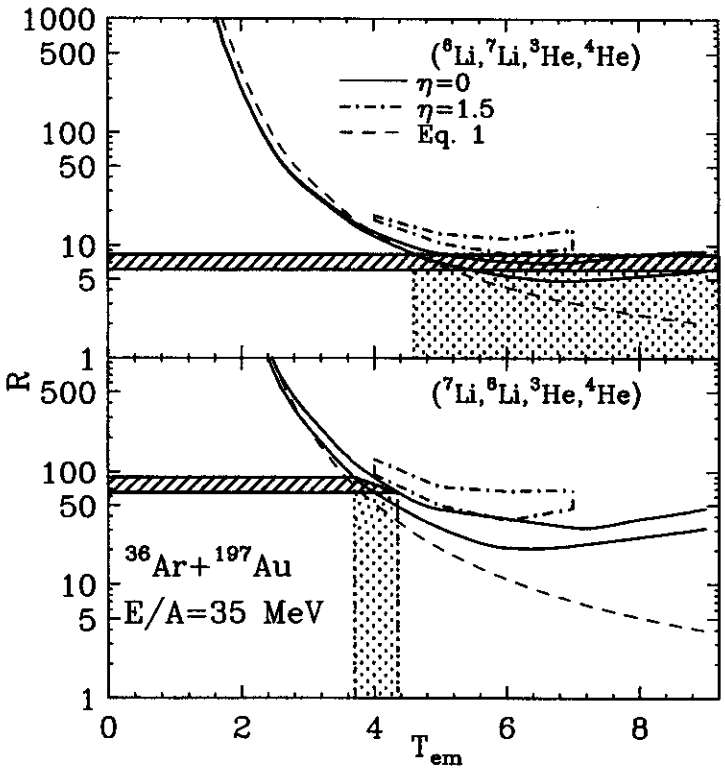

Figure 2: The isotope yield ratios derived from sequential calculations is plotted against the input temperature, T_{em}. The horizontal hatched areas indicate the measured isotope yield ratios and the vertical shaded areas indicate the range of the extracted isotope temperatures. See text for the detailed description of the solid, dot-dashed and dashed curves.

impact parameter with an average charged particle multiplicity of 2. The data presented here were obtained for a reduced impact parameter $\hat{b} \leq 0.3$.

Temperatures were extracted using two different sets of isotopes : (^{6}Li, ^{7}Li, ^{3}He, ^{4}He) which was also used in ref. [1] and a second set (^{7}Li, ^{8}Li, ^{3}He, ^{4}He). The experimental measured R are plotted as horizontal bars in Fig. 2.

A systematic uncertainty of 15% is assigned to the extracted values. The error bars take into account uncertainties in the moving source fits to extract the yield of all isotopes to high energy regions, possible contamination of the ^{7}Li energy spectra by the alpha decay of ^{8}Be (<4%) and the kinematic uncertainties arising from limited angular coverage in the measurement.

In the sequential calculations described in ref. [14,15] particles are assumed to be emitted at freeze-out by a thermalized source of temperature T_{em}. In these calculations, the population of an excited state of a nucleus at excitation energy E_i^*, spin J_i and mass number A_i and charge number Z_i was assumed to be of the form

$$P_i(A_i,\ Z_i,\ E_i^*,\ f,\ T_{em}) \propto (2J_i+1)A_i^{\eta} exp(-f\frac{V_i}{T_{em}} + \frac{Q_i}{T_{em}}) exp(-E_i^*/T_{em}) \qquad (5)$$

where V_i is the Coulomb barrier and Q_i separation energy. All the tabulated low lying discrete states as well as the unstable states in the continuum up to the maximum excitation energy of 4.6 AMeV were

included in the calculations. η was set to zero for the calculations published in ref. [15]. Calculations were performed with trial initial temperatures, T_{em}, ranging from 1 to 9 MeV in 1 MeV steps [15]. At each value of T_{em}, the factor f was adjusted to make the final charge distributions agree with the experimentally measured ones [15]. This latter requirement provides an essential constraint on the actual amount of sequential feeding in the calculations [7,14,17]. At each temperature, unknown spins and parities of tabulated discrete states included in the calculation were also randomly assigned and calculations were repeated 10 times to assess the uncertainties in the calculations.

Sequential decay calculations for isotope double ratios for the groups (^{6}Li, ^{7}Li, ^{3}He, ^{4}He) and (^{7}Li, ^{8}Li, ^{3}He, ^{4}He) are given in the upper and lower panels of Fig. 2, respectively. Two solid curves shown in each panel bound the range of values of R obtained by varying the unknown spins and parities of discrete states [15] as a function of the emission temperatures, T_{em}. From the intersection of the data and the calculations, the relative isotope yields of (^{6}Li, ^{7}Li, ^{3}He, ^{4}He) provide an isotope temperature, $T_{em} > 4.6$ MeV while the isotope yields for (^{7}Li, ^{8}Li, ^{3}He, ^{4}He) give T_{em}=4.0 $\pm$ 0.3 MeV. The temperature obtained in ref. [15] from the excited state populations of Lithium, Beryllium and Boron isotopes in the same reaction is 4.5 $\pm$ .5 MeV. This result is comparable to the temperatures extracted from the isotope ratios.

We have also investigated the influence the assumed charge to mass ratios of the thermalized emitting system on the isotope ratios. Decreasing the charge to mass ratios of the emitting system up to 20% changes the ratio R by less than 10%, well within the uncertainties of the present calculations. Similarly, we have investigated the pre-exponential term, A^{η}, in Eq. 5. The dot-dashed lines in Fig. 2 enclosed the upper and lower limits of the corresponding sequential decay calculations with η=1.5 (corresponding to the case of volume emission) for 4 MeV $\leq T_{em} \leq$ 7 MeV. Inclusion of this factor increases the calculated isotope yield ratios R by about 40% allowing only lower limits $T_{em} > 4.1$ MeV and $T_{em} >$ 6 MeV to be extracted for (^{7}Li, ^{8}Li, ^{3}He, ^{4}He) and (^{6}Li, ^{7}Li, ^{3}He, ^{4}He) isotope groups respectively. For surface emission, η=1 (not plotted in Fig. 2) the increase in R is slightly less, about 30% and the shift is correspondingly less. The sensitivity of the isotope temperatures to η represents an uncertainty that merits further study.

Using the procedure developed above, we have reanalyzed the data of ref. [1], taking the sequential decay effects explicitly into account. Calculations for the solid points in the left panel in Fig. 1 were performed for various emission temperatures T_{em} and factors f. From the calculations, optimal values for T_{em} and f were chosen which simultaneously reproduce measured isotope ratios R, obtained from the published [1] values of T_{LiHe} by inverting Eq. 1, and the corresponding charge distributions of ref. [18] which have been parameterized according to $Y(Z) \propto Z^{-\tau}$ with the τ values listed in Table 1. (This constraint on f is essential to constrain the relative yields of heavier particle unbound nuclei feeding the observed He and Li isotopes.) The sensitivity to $E^*_{\rm max}$ was assessed by varying it over the range 1 MeV $\leq E^*_{\rm max} \leq$ 5 MeV. The solid points at $< E_o/A_o > \leq$ 10 MeV in the right panel of Fig. 1 represent average values for T_{em} taking the variation of T_{em} with $E^*_{\rm max}$ and the sensitivity to unknown spins and parities of tabulated discrete states into account. At $< E_o/A_o >=$ 11.6 and 13.2 MeV, no upper limit to the temperature was established and values at $< E_o/A_o >=$ 15.6 MeV are not plotted because the corresponding charge distributions could not be reproduced via Eq. 5.

The extracted values for T_{em} are lower than those reported for T_{LiHe} at $< E_o/A_o > \leq$ 10 MeV. They increase regularly with $< E_o/A_o >$ and unlike ref. [1] show no plateau in the region 2 MeV $\leq$ $< E_o/A_o > \leq$ 10 MeV. Since uncertainties in T_{em} are relatively small at $< E_o/A_o > \leq$ 10 MeV, differences between T_{em} and T_{HeLi} reflect the fact that a constant normalization factor ($T_{em} = 1.2 * T_{HeLi}$) used in ref.

[1] is not a good approximation. At larger values of $< E_o/A_o >> 10$ MeV, the yield ratio R is less sensitive to T_{em} than to the uncertainties in the secondary decay correction. One cannot extract sufficiently accurate temperatures in this energy domain to definitively establish a constant heat capacity characteristic of a gaseous phase as reported by ref. [1].

a. Present Address: Physics Department, Brookhaven National Laboratory, Upton, Long Island, NY 11973.
b. Present Address: Physics Department University of Texas, El Paso, TX 79968.
c. Present Address: Chalk River National Laboratories, Chalk River, Ontario, Canada K0J 1J0.
d. Present Address: IUCF and Chemistry Department, Indiana Univ. Bloomington IN.47405.
e. Present Address: National Laboratory for High energy Physics, 1-1 Oho, Tsukuba, Ibaraki 305. Japan.
f. Present Address: Lawrence Berkeley Laboratory, Berkeley CA 94720.
g. Present Address: Cyclotron Institute, Texas A&M University. College Station, TX 77843.
h. Department of Physics, University of Wisconsin, Madison, WI 53706, USA

References

1. J. Pochodzalla et al., Phys. Rev. Lett. 75, 1040 (1995).
2. S. Albergo et al., Nuovo Cimento A89, 1 (1995).
3. D.H.E.Gross,Phys.Rev.Lett.56,1544(1986).
4. J.P. Bondorf et al., Nucl. Phys. A443 (1985) 321; Nucl. Phys. 460 A444 (1986).
5. C. Schwarz et. al. Phys. Rev. C 48, 676 (1993).
6. J. Pochodzalla et al., Phys. Rev. C 35, 1695 (1987).
7. T.K. Nayak et al., Phys. Rev. C 45, 132 (1992).
8. G.J. Kunde et al., Phys. Lett. B 272, 202 (1991).
9. C.B. Chitwood et. al., Phys. Lett. B 172, 27 (1986).
10. H. Xi et al., Nucl. Phys. A552, 281 (1993).
11. D.J. Morrissey, W. Benensen, W.A. Friedman, Ann. Rev. Nucl. Part. Sci. 44, 27 (1994) and references therein.
12. W.C. Hsi et al., Phys. Rev. Lett. 73 , 3367 (1994).
13. K. G. R. Doss et al, Phys. Rev. Lett. 59, 2720 (1987).
14. F. Zhu et al., Phys. Lett. B 282, 299 (1992).
15. F. Zhu et al., Phys. Rev. C 52, 784 (1995).
16. R.T. DeSouza, Nucl. Inst. and Meth. A295, 109 (1990).
17. H.M. Xu et al., Phys. Lett. B 182, 155 (1986).
18. C.A. Ogilvie et. al., Nucl. Phys. A553, 255c (1993).

TWO–PROTON CORRELATIONS FOR $^{16}O + ^{197}Au$ COLLISIONS AT E/A = 200 MeV

S.J. Gaff, C.K. Gelbke, W. Bauer, F.C. Daffin, T. Glasmacher, E. Gualtieri, K. Haglin, D.O. Handzy, S. Hannuschke, M.J. Huang, G.J. Kunde, R. Lacey[a], W.G. Lynch, L. Martin, C.P. Montoya[b], R. Pak, S. Pratt, N. Stone, M.B. Tsang, A.M. Vander Molen, G.D. Westfall, and J. Yee

Two protons, emitted at small relative momentum from an excited system, can be used to obtain information about the space–time characteristics of the emitting source formed in nuclear collisions [1–18]. Calculations with the Boltzmann–Uehling–Uhlenbeck (BUU) transport equation have been rather successful [9–11,14] in reproducing inclusive two–proton correlation functions at beam energies below approximately E/A $\approx$ 100 MeV, but such calculations predicted too large correlations for inclusive collisions of $^{40}Ar + ^{197}Au$ at E/A = 200 MeV [14]. By measuring $^{16}O + ^{197}Au$ collisions at E/A = 200 MeV, we hope to collect more data in the area of this discrepency.

The experiment used a beam of ^{16}O ions at E/A = 200 MeV, the highest energy per nucleon possible from the K1200 cyclotron. Coincident protons were detected by a 56–element high–resolution hodoscope [19,20] attached to the MSU 4π Array [21] at $< \Theta_{lab} > = 38°$. Events were written on tape when they satisfied the trigger condition of at least two detectors of the 56–element hodoscope and at least three detectors of the 4π–Array firing. This trigger eliminated the most peripheral collisions, but otherwise accepted a broad range of impact parameters. Due to a major power outage, the experiment had to be ended prematurely, and the statistics collected were insufficient to allow significant cuts on impact parameter. Thus we can only present inclusive two–proton correlation functions.

The solid points in Fig. 1 show the measured energy spectrum of protons emitted at polar angles Θ_{lab} = 30° – 45°. The solid curve represents the corresponding energy spectrum predicted by the BUU calculations [13,22–24]. The calculations were filtered for the experimental acceptance and energy thresholds. At energies near the Coulomb barrier BUU calculations over predict the proton yield. Such an over prediction of the proton yields at low energies has been noted previously and attributed to the neglect of light cluster formation [18,25,26]. Light clusters are expected to be predominantly formed in densely populated regions of phase space, thus reducing the flux of free nucleons.

Two–proton correlation functions, $1 + R(q)$, are presented in Fig. 2. The experimental two–proton correlation function, shown by points, was defined in terms of the two–proton coincidence yield, $Y_2(\mathbf{p}_1, \mathbf{p}_2)$, and a background yield, $Y_{back}(\mathbf{p}_1, \mathbf{p}_2)$, obtained by the event–mixing technique [27]

$$\sum Y_2(\mathbf{p}_1, \mathbf{p}_2) = C[1 + R(q)] \sum Y_{back}(\mathbf{p}_1, \mathbf{p}_2). \quad (1)$$

Here q is the (invariant) magnitude of the relative momentum four–vector. For a given experimental gating condition, the sums of each side of Eq. (1) extend over all proton energies and detector combinations of the 56–element hodoscope corresponding to each q–bin. The normalization constant C is determined by the requirement that $R(q)$ vanish for large q, where final state interactions between the emitted protons are negligible. Specifically we normalized both experimental and theoretical correlation functions such that $< R(q) > = 0$ for 60 MeV/c$\leq q \leq$80 MeV/c.

Theoretical two–proton correlation functions (shown by curves in Fig. 2) were calculated with the Koonin–Pratt formalism which relates the one–body phase space distribution with the correlation function [1,6,10,11]. The upper panel of Fig. 2 presents the energy–integrated correlation function for all protons

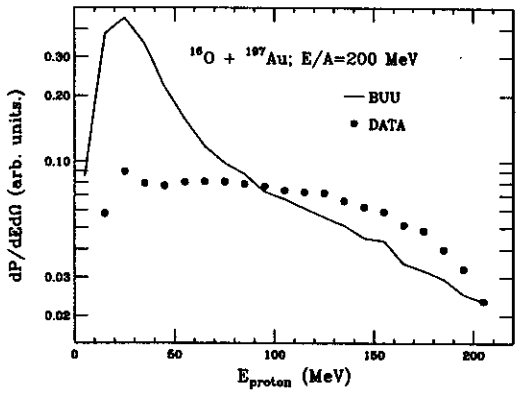

Figure 1: Energy spectra of protons measured in the laboratory rest frame at $\Theta_{lab} = 30° - 45°$ for collisions of $^{16}O + ^{197}Au$ at E/A = 200 MeV (solid points) are compared with the prediction of BUU (solid line). To allow a better comparison of shapes, the relative normalization between experimental and theoretical energy spectra was chosen to give equal areas for $E_{proton} > 50$ MeV.

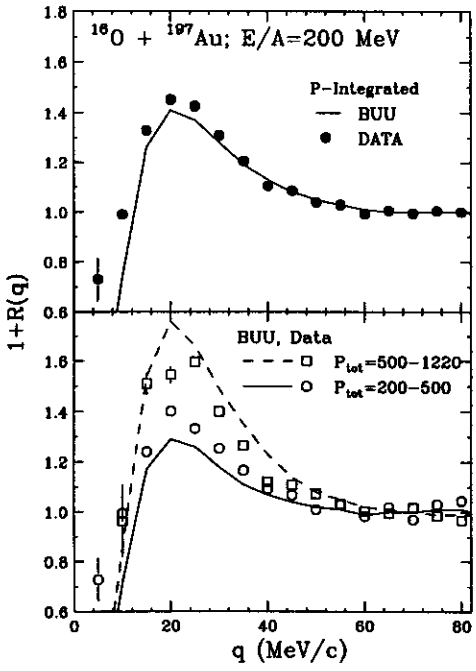

Figure 2: Two–proton correlation functions for collisions of $^{16}O + ^{197}Au$ at E/A = 200 MeV. The top panel shows the energy–integrated correlation function, and the bottom panel shows correlation functions for proton pairs selected by the indicated cuts on their total momentum.

detected by the 56–element hodoscope with laboratory energy above 10 MeV and below 200 MeV. The lower panel shows correlation functions selected by two different cuts on $P_{tot} = | p_1 + p_2 |$, the total momentum of the detected proton pair in the center–of–momentum frame of projectile and target.

The BUU calculations reproduce the magnitude of the energy–integrated correlation function (top panel), but they predict too strong a dependence on P_{tot} (bottom panel). The calculations under predict the magnitude of the correlation functions measured for the low–momentum gate, 200 MeV/c $\leq P_{tot} \leq$ 500 MeV/c, and they over predict it for the high–momentum gate, 500 MeV/c $\leq P_{tot} \leq$ 1220 MeV/c.

In summary, proton energy spectra and two–proton correlation functions were measured at $< \Theta_{lab} >$ = 38° for ^{16}O + ^{197}Au collisions at E/A = 200 MeV. The single particle yield for the low–energy protons has a flat slope that is not reproduced well by the BUU transport model. The momentum–integrated correlation function agrees well with the BUU calculations, and the momentum–gated correlation functions show a definite dependence on the momentum of the proton pair.

a. Present address: Department of Chemistry, State University of New York, Stony Brook, NY 11776
b. Present address: Merrill Lynch, World Financial Center, North Tower, New York, NY 10281

References

1. S.E. Koonin, Phys. Lett. 70B, 43 (1977).
2. W.G. Lynch, C.B. Chitwood, M.B. Tsang, D.J. Fields, D.R. Klesch, C.K. Gelbke, G.R. Young, T.C. Awes, R.L. Ferguson, F.E. Obenshain, F. Plasil, R.L. Robinson, and A.D. Panagiotou, Phys. Rev. Lett. 51, 1850 (1983).
3. D.H. Boal and J.C. Shillcock, Phys. Rev. C 33, 549 (1986).
4. D.H. Boal and H. DeGuise, Phys. Rev. Lett. 57, 2901 (1986).
5. Z. Chen, C.K. Gelbke, W.G. Gong, Y.D. Kim, W.G. Lynch, M.R. Maier, J. Pochodzalla, M.B. Tsang, F. Saint–Laurent, D. Ardouin, H. Delagrange, H. Doubre, J. Kasagi, A. Kyanowski, A. Péghaire, J. Péter, E. Rosato, G. Bizard, F. Lefébvres, B. Tamain, J. Québert, and Y.P. Viyogi, Phys. Rev. C 36, 2297 (1987).
6. S. Pratt and M.B. Tsang, Phys. Rev. C 36, 2390 (1987).
7. T.C. Awes, R.L. Ferguson, F.E. Obenshain, F. Plasil, G.R. Young, S. Pratt, Z. Chen, C.K. Gelbke, W.G. Lynch, J. Pochodzalla, and H.M. Xu, Phys. Rev. Lett. 61, 2665 (1988).
8. D.H. Boal, C.K. Gelbke, and B.K. Jennings, Rev. Mod. Phys. 62, 553 (1990).
9. W.G. Gong, W. Bauer, C.K. Gelbke, N. Carlin, R.T. de Souza, Y.D. Kim, W.G. Lynch, T. Murakami, G. Poggi, D. Sanderson, M.B. Tsang, H.M. Xu, S. Pratt, D.E. Fields, K. Kwiatkowski, R. Płaneta, V.E. Viola, Jr., and S.J. Yennello, Phys. Rev. Lett. 65, 2114 (1990).
10. W.G. Gong, W. Bauer, C.K. Gelbke, and S. Pratt, Phys. Rev. C 43, 781 (1991).
11. W.G. Gong, C.K. Gelbke, W. Bauer, N. Carlin, R.T. de Souza, Y.D. Kim, W.G. Lynch, T. Murakami, G. Poggi, D.P. Sanderson, M.B. Tsang, H.M. Xu, D.E. Fields, K. Kwiatkowski, R. Płaneta, V.E. Viola, Jr., S.J. Yennello, and S. Pratt, Phys. Rev. C 43, 1804 (1991).
12. D. Rebreyend, F. Merchez, B. Norén, E. Andersen, M. Cronqvist, J.C. Gondrand, H.A. Gustafsson, B. Jäger, B. Jakobsson, B. Khelfaouli, S. Kox, A. Kristiansson, G. Lövhöiden, S. Mattson, T.F. Thorsteinsen, M. Westenius, and L. Westerberg, Phys. Rev. C 46, 2387 (1992).
13. W. Bauer, C.K. Gelbke, and S. Pratt, Annu. Rev. Nucl. Part. Sci. 42, 77 (1992).
14. G.J. Kunde, J. Pochodzalla, E. Berdermann, B. Berthier, C. Cerruti, C.K Gelbke, J. Hubele, P. Kreutz, S. Leray, R. Lucas, U. Lynen, U. Milkau, C. Ngo, C.H. Pinkenburg, G. Raciti, H. Sann, and W. Trautmann, Phys. Rev. Lett. 70, 2545 (1993).
15. M.A. Lisa, C.K. Gelbke, W. Bauer, P. Decowski, W.G. Gong, E. Gualtieri, S. Hannuschke, R. Lacey, T. Li, W.G. Lynch, C.M. Mader, G.F. Peaslee, T. Reposeur, A.M. Vander Molen, G.D. Westfall, J. Yee, and S.J. Yennello, Phys. Rev. Lett. 70, 3709 (1993).
16. M.A. Lisa, C.K. Gelbke, P. Decowski, W.G. Gong, E. Gualtieri, S. Hannuschke, R. Lacey, T. Li, W.G. Lynch, G.F. Peaslee, S. Pratt, T. Reposeur, A.M. Vander Molen, G.D. Westfall, J. Yee, and S.J. Yennello, Phys. Rev. Lett. 71, 2863 (1993).
17. D.O. Handzy, M.A. Lisa, C.K. Gelbke, W. Bauer, F.C. Daffin, P. Decowski, W.G. Gong, E. Gualtieri, S. Hannuschke, R. Lacey, T. Li, W.G. Lynch, C.M. Mader, G.F. Peaslee, T. Reposeur, S. Pratt, A.M. Vander Molen, G.D. Westfall, J. Yee, and S.J. Yennello, Phys. Rev C 50, 858 (1994).

18. D.O. Handzy, Ph.D. thesis, Michigan State University (1995).
19. W.G. Gong, Y.D. Kim, G. Poggi, Z. Chen, C.K. Gelbke, W.G. Lynch, M.R. Maier, T. Murakami, M.B. Tsang, H.M. Xu, and K. Kwiatkowski, Nucl. Instrum. Methods A268, 190 (1988).
20. W.G. Gong, N. Carlin, C.K. Gelbke, and R. Dayton, Nucl. Instrum. Methods A287, 639 (1990).
21. G.D. Westfall, J.E. Yurkon, J. van der Plicht, Z.M. Koenig, B.V. Jacak, R. Fox, G.M. Crawley, M.R. Maier, and B.E. Hasselquist, Nucl. Instrum. Methods A238, 347 (1985).
22. W. Bauer, Nucl. Phys. A471, 604 (1987).
23. B.A. Li and W. Bauer, Phys. Rev. C 44, 450 (1991).
24. B.A. Li, W. Bauer, and G.F. Bertsch, Phys. Rev. C 44, 2095 (1991).
25. D.O. Handzy, W. Bauer, F.C. Daffin, S.J. Gaff, C.K. Gelbke, T. Glasmacher, E. Gualtieri, S. Hannuschke, M.J. Huang, G.J. Kunde, R. Lacey, T. Li, M.A. Lisa, W.J. Llope, W.G. Lynch, L. Martin, C.P. Montoya, R. Pak, G.F. Peaslee, S. Pratt, C. Schwarz, N. Stone, A.M. Vander Molen, G.D. Westfall, J. Yee, and S.J. Yennello, Phys. Rev. Let. 75, 2916 (1995).
26. W.G. Gong, P. Danielewicz, C.K. Gelbke, N. Carlin, R.T. de Souza, Y.D. Kim, W.G. Lynch, T. Murakami, G. Poggi, M.B. Tsang, H.M. Xu, S. Pratt, K. Kwiatkowski, V.E. Viola, Jr., S.J. Yennello, and J.C. Shillcock, Phys. Rev. C 47, R429 (1993).
27. M.A. Lisa, W.G. Gong, C.K. Gelbke, and W.G. Lynch, Phys. Rev. C 44, 2865 (1991).

UNDERSTANDING PROTON EMISSION IN CENTRAL HEAVY–ION COLLISIONS

D.O. Handzy, W. Bauer, F.C. Daffin, S.J. Gaff, C.K. Gelbke, T. Glasmacher, E. Gualtieri, S. Hannuschke, M.J. Huang, G.J. Kunde, R. Lacey[a], T. Li, M.A. Lisa[b], W. J. Llope[c], W.G. Lynch, L. Martin, C.P. Montoya[d], R. Pak, G.F. Peaslee[e], S. Pratt, C. Schwarz[f], N. Stone, M.B. Tsang, A.M. Vander Molen, G.D. Westfall, J. Yee, and S.J. Yennello[g]

Two–proton correlation functions provide a means for viewing the space–time development of heavy–ion collisions [1–3]. Semi–classical simulations based on the Boltzmann–Uehling–Uhlenbeck (BUU) model are thought to provide a reasonable picture of the global dynamics of intermediate–energy nucleus–nucleus collisions [4]. BUU calculations were successful in reproducing two–proton correlation functions measured at energies below about 100 MeV per nucleon [5,6–9]. Rather surprisingly, the model failed to explain inclusive measurements for ^{40}Ar + ^{197}Au collisions at 200 MeV per nucleon [9] where it should have been on firm theoretical ground.

In this report, we present experimental results for central collisions of ^{36}Ar + ^{45}Sc at E/A = 80, 120 and 160 MeV. BUU calculations predict shorter emission time scales and hence smaller apparent source sizes as the beam energy is increased. These predictions are not confirmed experimentally, and clear discrepancies between theory and experiment are observed at the two higher energies. We argue that the failure of the model may be attributable to delayed emission from particle unbound states – a quantum effect not included in the BUU theory.

Beams, from the K1200 cyclotron, of ^{36}Ar ions with 80, 120, and 160 MeV per nucleon energy were focused on ^{45}Sc targets. Charged particles were detected in the MSU 4π Array [10]. Particles stopped in the slow E–scintillators were identified by particle type and energy, with calibration uncertainty of about 10%. One module of the 4π Array, centered at θ_{lab} = 38°, was replaced by a hodoscope [11,12] of 56 ΔE-E-telescopes. Both two–proton coincidence and singles events in the hodoscope were recorded in coincidence with data from the 4π Array. An impact parameter scale was established from the total transverse kinetic energy [7,13] measured in the 4π–Array, and central collisions were selected by the cut $b/b_{max} \leq 0.3$.

The solid points in Fig. 1 show the singles energy spectra of protons detected at $\langle\theta_{lab}\rangle$ = 31°; histograms show BUU predictions. The BUU calculations over predict the low-energy proton yield, but they reproduce the approximate shape of the high–energy tail. The over prediction of proton yields at low energy has been observed before and attributed to the model's inability to treat the formation of bound clusters [14]. Clusters should form preferentially in regions of phase space where the nucleon population density is high, hence more protons should be "lost" to bound clusters at lower than at higher proton energy.

Figure 2 shows experimental (points) and theoretical (curves) correlation functions gated on total center–of–mass momentum, $P_{cm} = |p_1 + p_2|$, of the detected proton pairs. The experimental correlation function, 1+R(q), was defined in terms of the two–proton coincidence yield, $Y_2(\mathbf{p}_1, \mathbf{p}_2)$, and the proton singles yield, $Y_1(\mathbf{p})$:

$$\sum Y_2(\mathbf{p}_1, \mathbf{p}_2) = C[1 + R(q)] \sum Y_1(\mathbf{p}_1) Y_1(\mathbf{p}_2). \quad (1)$$

Here, p_i is the momentum of proton i, and q is the (invariant) magnitude of the relative momentum four–vector. For a given experimental gating condition, the sums on each side of Eq. (1) extend over all

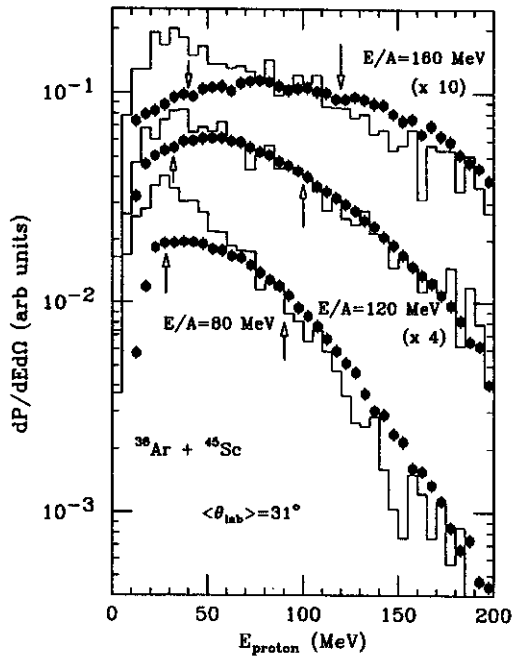

Figure 1: Laboratory frame proton energy spectra measured at θ_{lab}=31° for central ($b/b_{max} \leq 0.3$) collisions of ^{36}Ar + ^{45}Sc at E/A=80, 120, and 160 MeV (solid points) are compared with the predictions of BUU (histograms). Relative normalization gives equal areas for measured and predicted spectra for $E_{proton} \geq 50$ MeV. The arrows indicate average values of E^{lab}_{proton} corresponding to low and high momentum cuts used to analyze the correlation function in Fig. 2

proton energies and detector combinations of the 56–element hodoscope corresponding to each q–bin. The normalization constant C is defined such that $\langle R(q) \rangle = 0$ for 60 MeV/c $\leq$ q $\leq$ 80 MeV/c.

Theoretical two–proton correlation functions were calculated with the Koonin–Pratt formula which relates the one-body phase space distribution (predicted by BUU) with the correlation function [1,3,5,6]. The BUU calculations (filtered for experimental acceptance and energy thresholds) were performed with parameters that successfully described correlation functions measured at E/A < 100 MeV. The BUU calculations reproduce the data at E/A = 80 MeV [7], but fail to reproduce either the magnitude or the weak dependence on P_{cm} at the two higher energies .

The BUU predictions can be understood from the proton emission rates, dP/dt, calculated for central ^{36}Ar + ^{45}Sc collisions; see Fig. 3. At 80 MeV per nucleon, the BUU calculations predict the existence of a long–lived residue [7] which cools by particle emission. In contrast, at the higher energies, a fast flash of nucleon emission is predicted, without residue. While this drastically different scenario leaves no obvious signal in the single–particle spectra shown in Fig. 1, it results in enhanced two–proton correlations – at variance with the data. The near–degeneracy of low and high momentum correlation functions at E/A = 160 MeV, also not reproduced by the calculations, may indicate that low and high–energy protons are emitted on similar time scales, and that there is no evaporative cooling of the source.

The lack of fragment formation in the current BUU formalism may be responsible for its substantial over prediction of the correlation functions at E/A = 120 and 160 MeV. At the energies under consideration, high–lying particle–unstable states may play an important role in proton production by extending the time scale, τ, over which protons are emitted. Such delayed emissions are known to exist [8,15], but their magnitude is unknown. We have performed a schematic simulation of such effects by taking a fraction,

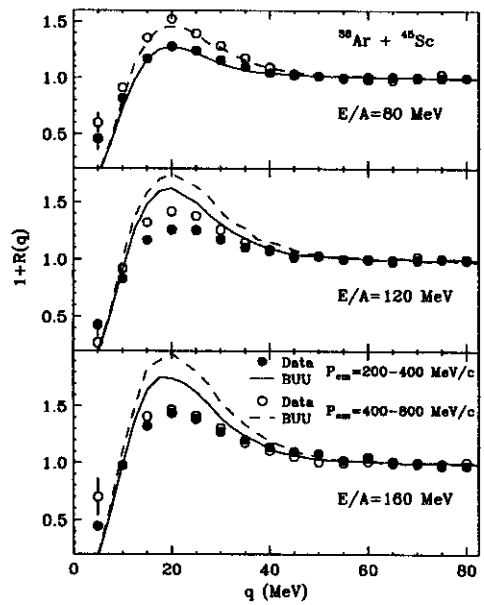

Figure 2: Two-proton correlation functions for central collisions of ^{36}Ar + ^{45}Sc at E/A = 80 MeV (top), 120 MeV (middle) and 160 MeV (bottom). The momentum cuts employed are indicated in the figure.

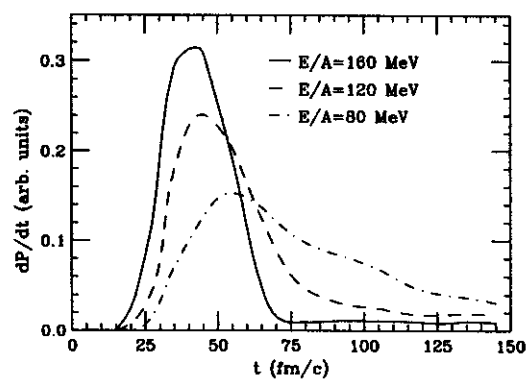

Figure 3: Proton emission rates predicted by BUU calculations for central ^{36}Ar+ ^{45}Sc collisions at E/A=80, 120 and 160 MeV.

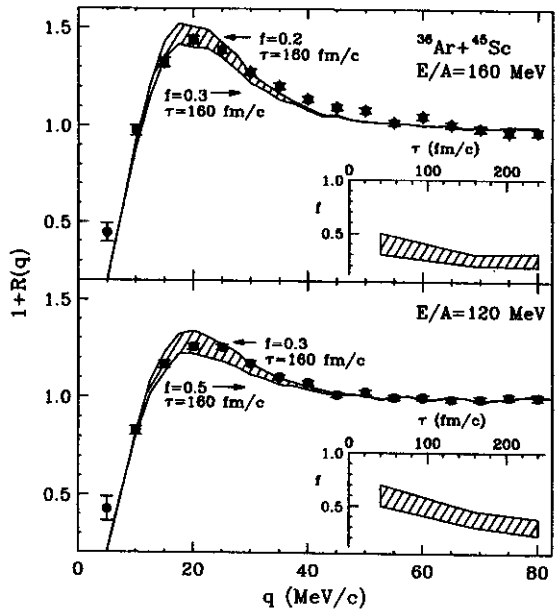

Figure 4: Two proton correlation functions (for low–momentum cut) for central collisions of ^{36}Ar + ^{45}Sc at E/A = 160 MeV (top panel) and 120 MeV (bottom panel). Data are shown by points; calculations are described in the text. The inserts depict the parameter ambiguity.

f, of the protons predicted to be emitted by BUU and delaying their emission for a time τ, statistically distributed according to $dP/dt = e^{-t/\tau}$. We chose values of τ between 40 to 240 fm/c, corresponding to resonances of widths between approximately 0.8 – 5 MeV. Examples of simulations which reproduce the magnitude of the experimental correlation function at E/A = 160 and 120 MeV are shown in the top and bottom panels of Fig. 4. The parameters for these calculations are indicated in the figure. The insets indicate the ranges of τ and f which give similarly good agreement with the data; to some extent, smaller fractions, f, of delayed particles can be compensated by longer delay times, τ.

While the correlation functions are consistent with a delayed proton–emission component, the magnitude of this component is uncertain and not well determined by our schematic simulation [16]. In order to assess whether the range of parameters shown in the insets of Fig. 4 is compatible with statistical expectations, we have performed calculations with the statistical codes Firestreak [17] and FREESCO [18] to estimate sequential–decay contributions to the proton yield. For a single source containing 81 nucleons, using ρ_f=ρ_o/8 and T_f = 8 MeV, the Firestreak model predicts that about 50% of the emitted protons come from resonances; the FREESCO prediction is slightly less than 20% [19]. This range, from the insets of Fig. 4, is qualitatively consistent with values of τ between 50 and 200 fm/c, or widths between 1 and 4 MeV, which are typical of light resonances such as ^{5}Li* and α*.

In summary, two–proton correlation functions were measured for central ^{36}Ar + ^{45}Sc collisions at beam energies of 80, 120, and 160 MeV per nucleon. For the two higher beam energies, the BUU transport theory predicts too large correlations, i.e. proton emission from a more compact space–time geometry than observed experimentally. This deficiency of the theory is likely due to its inability to treat the population of particle unbound resonances and their decay via delayed particle emission. We conclude that proton (and hence nucleon) production in medium–energy heavy–ion collisions is not yet well understood theoretically.

a. Present address: Department of Chemistry, State University of New York, Stony Brook, NY 11776
b. Present address: Lawrence Berkeley Laboratory, Berkeley, CA 94720
c. Present address: T.W. Bonner Nuclear Laboratory, Rice University, Houston, TX 77251
d. Present address: Merrill Lynch, World Financial Center, North Tower, New York, NY 10281
e. Present address: Department of Chemistry,
f. Present address: GSI, Postfach 110552; D–64220 Darmstadt, Germany
g. Present address: Cyclotron Institute, Texas A&M University, College Station, TX 77843

References

1. S. E. Koonin *et al.*, Phys. Lett. 70B, 43 (1977).
2. D. H. Boal, C. K. Gelbke, and B. K. Jennings, Rev. Mod. Phys. 62, 553 (1990).
3. W. Bauer, C. K. Gelbke, and S. Pratt, Annu. Rev. Nucl. Part. Sci. 42, 77 (1992).
4. G.F. Bertsch and S. Das Gupta, Phys. Rep. 160, 189 (1988).
5. W. G. Gong *et al.*, Phys. Rev. C 43, 1804 (1991).
6. W. G. Gong *et al.*, Phys. Rev. C 43, 781 (1991).
7. M.A. Lisa *et al.*, Phys. Rev. Lett. 70, 3709 (1993); D.O. Handzy *et al.*, Phys. Rev. C 50, 858 (1994).
8. J. Pochodzalla *et al.*, Phys. Rev. C 35, 1695 (1987).
9. G.J. Kunde *et al.*, Phys. Rev. Lett. 70, 2545 (1993).
10. G.D. Westfall *et al.*, Nucl. Instrum. Methods A238, 347 (1985).
11. A. Elmaani *et al.*, Phys Rev. C 48, 2864 (1993).
12. W.G. Gong *et al.*, Nucl. Instrum. Methods A 268, 190 (1988); Nucl. Instrum. Methods A 287, 639 (1990).
13. L. Phair *et al.*, Nucl. Phys. A548, 489 (1992); Nucl. Phys. A564, 453 (1993).
14. W.G. Gong *et al.*, Phys. Rev. C 47, R429 (1993).
15. G.J. Kunde *et al.*, Phys. Lett. B 272, 202 (1991).
16. Slightly larger resonance contributions are needed at E/A=120 MeV than at 160 MeV; because of the schematic nature of our calculations, this result should not be over interpreted.
17. G.D. Westfall *et al.*, Phys. Rev. Lett. 37, 1202 (1976); J. Gosset *et al.*, Phys. Rev. C 18, 844 (1978).
18. G. Fái and J. Randrup, Nucl. Phys. A 381, 557 (1982); Nucl. Phys. A 404, 551 (1983).
19. The two predictions differ because FREESCO incorporates more resonances than Firestreak; for details see refs. [22] and [23].

MASS DEPENDENCE OF DIRECTED COLLECTIVE FLOW

M.J. Huang[a], R.C. Lemmon[a], F. Daffin[a], W.G. Lynch[a], C. Schwarz[ad], M.B. Tsang[a], C. Williams[a], P. Danielewicz[a], K. Haglin[a], W. Bauer[a], N. Carlin[f], R.J. Charity[c], R.T. de Souza[e], C.K. Gelbke[a], W.C. Hsi[ae], G.J. Kunde[ad], M-C. Lemaire[b], M.A. Lisa[a], U. Lynen[d], G.F. Peaslee[a], J. Pochodzalla[d], H. Sann[d], L.G. Sobotka[c], S.R. Souza[b], and W. Trautmann[d]

Information about the equation of state can be extracted from the collective flow of nuclear matter deflected sidewards from the hot and dense region formed by the overlap of projectile and target nuclei [1,2]. This flow reflects the interplay of collective and random motions. For a thermalized system, the random motions of emitted fragments are dictated by the thermal energy, which is independent of mass. Contributions to the fragment energy due to collective motion, on the other hand, increase linearly with mass, making the flow more easily observed for heavier fragments [3,4].

Measurements of light charged particle (p,d,t,α) flow confirm that transverse collective flow increases with mass [3] but a systematic understanding of the dependence of collective flow upon fragment mass is lacking. Such information is essential for quantitative flow extraction at incident energies E/A$\leq$250 MeV, where fragments remove much of the total mass [5,6]. We have made the first quantitative examination of the mass dependence of collective flow which includes intermediate mass fragments up to Z=6. These effects are explored with the mass-asymmetric ^{84}Kr+ ^{197}Au system which allows clear distinctions between different parameterizations of the nuclear EOS.

In the experiment, 5 mg/cm^2 thick ^{197}Au targets were bombarded with 200A MeV ^{84}Kr beams of the Laboratoire National SATURNE at Saclay. The emitted charged particles were detected with the combined Miniball/ Wall array [7]. Flow analyses were performed within an energy gate of E/A = 20-75 MeV which took the minimum energy for ^{3}He and α separation and the range for energetic protons in the Miniball detectors into account. An impact parameter scale was constructed from the total detected charged particle multiplicity and normalized via cross section measurements [5]. Further details about the experiment can be found in Ref. [5].

The in-plane component of the directed flow is usually extracted by techniques [8], wherein the momenta of detected particles are projected onto an experimentally determined reaction plane . Experimentally extracted reaction planes generally fluctuate about the true reaction plane for each event [9], however, introducing uncertainties in the extracted transverse momenta. Corrections for this reaction plane dispersion may be applied, but have uncertainties that become especially large when the flow is small [10].

To avoid such uncertainties, another technique has been proposed which involves constructing appropriate mean products of the measured momenta [11]. In this technique, the inner product $p_\nu^\perp(y_\nu) \cdot p_\mu^\perp(y_\mu)$ between the transverse momentum $p_\nu^\perp(y_\nu)$ of a particle of type ν at rapidity y_ν and the transverse momentum $p_\mu^\perp(y_\mu)$ of a particle of type μ at rapidity y_μ is averaged over the transverse momenta of the two particles. The random fluctuations of the transverse momenta about the collective mean values then average to zero leaving only the collective mean values. Choosing a coordinate system in which the non-vanishing mean collective transverse momenta lie along the x axis, this average inner product becomes [11]:

$$\langle p_\nu^\perp(y_\nu) \cdot p_\mu^\perp(y_\mu) \rangle \simeq \langle p_\nu^x(y_\nu) \rangle \langle p_\nu^x(y_\nu) \rangle. \quad (1)$$

Momentum conservation gives rise to further correlations between particle transverse momenta, modifying Eq. (1) to read [11]:

$$\langle p_\nu^\perp(y_\nu)\cdot p_\mu^\perp(y_\mu)\rangle \simeq \langle \quad p_\nu^x(y_\nu)\rangle\langle p_\nu^x(y_\nu)\rangle \\ -\alpha\langle p_\nu^{\perp^2}(y_\nu)\rangle\langle p_\mu^{\perp^2}(y_\mu)\rangle \qquad (2)$$

where $\alpha^{-1} \simeq \langle\sum_\mu p_\mu^{\perp^2}\rangle$ [11] and the sum runs over all emitted particles. (Since the experimental detection efficiency in the present experiment is less than one, the value for α^{-1} used in Eq. (2) was obtained by rescaling the experimental value for α^{-1} by the ratio of the total to the detected mass [12].) Final state interactions and apparatus non-uniformities can influence the extraction of the mean transverse momenta [11]; corrections have been made for these effects following ref. [11] but make little difference to the final results presented here.

Mean two-fragment inner products $\langle p_\nu^\perp(y_\nu)\cdot p_\mu^\perp(y_\mu)\rangle$ are then constructed for each possible pair of particle types with $1\leq Z_1, Z_2 \leq 6$ and selected bins of normalized rapidity, $y_n = y_{cm}/y_{beam}$. Eq. (2) is then solved by matrix diagonalization to obtain initial values for $\langle p_\nu^x(y_\nu)\rangle$ in the different rapidity bins [11]. Final values for $\langle p_\nu^x(y_\nu)\rangle$ are obtained by a least squares minimization procedure in which the $\langle p_\nu^x(y_\nu)\rangle$ on the r.h.s. of Eq. (2) are varied from their initial values so as to accurately satisfy Eq. (2). This procedure permitted an assessment of the uncertainties in the values for $\langle p_\nu^x(y_\nu)\rangle$.

Data were analyzed for two impact parameter gates: 1≤b≤3 fm and 4≤b≤6 fm. Within these gates, analyses were performed for particles with $-0.2 \leq y_n \equiv y/y_{beam} \leq 0.2$ in the center of momentum (c.m.) frame where deficiencies in the Miniball acceptance cause few distortions. The suitability of this criterion is illustrated for alpha particles in Fig. 1(a) where thermal model simulations for the mean transverse momenta of are shown with (filtered) and without (unfiltered) corrections for the experimental acceptance; this criterion is similarly suitable for the other analyzed particles as well. (Further details of these simulations are given below.) Measured mean transverse momenta per nucleon $\langle p^x/A\rangle$, shown in Fig. 1(b) for protons and Be fragments at 4≤b≤6 fm, reveal enhanced transverse momenta for heavier particles, consistent with trends observed in previous studies [3,4]. Near $y_n = 0$, the data in Fig. 1(b) are linear and well characterized by the collective flow, $F = d\langle p^x/A\rangle/dy_n$, which can be easily extracted via a linear least-squares fit near mid-rapidity. (Note that $\langle p_x/A\rangle$ does not cross zero at $y_n = 0$ for asymmetric systems.)

The flow per nucleon, $d\langle p^x/A\rangle/dy_n$, is shown as a function of fragment mass in Fig. 2 for the two impact parameter gates. Not surprisingly, the flow per nucleon is larger for the more peripheral gate. The flow increases monotonically with mass for Z≤2, consistent with previous measurements [3,4,13]. For fragments with Z>2, however, the flow is approximately independent of mass. This is the first time that the mass dependence of directed flow has been observed for intermediate mass fragments with sufficient statistics to examine this dependence in detail.

To examine the interplay between collective and thermal motion more quantitatively, we have simulated the velocity distributions of the fragments with a thermal expression of the form

$$P(\mathbf{v}) = \int d\mathbf{v}\mathcal{F}(\mathbf{v}_{coll})\mathcal{G}(\mathbf{v}_{th})\delta(\mathbf{v}-\mathbf{v}_{coll}-\mathbf{v}_{th}). \qquad (3)$$

Here, we assume a collective velocity distribution of Gaussian form $\mathcal{F}(\mathbf{v}_{coll}) \propto exp(-\sum_i [\mathbf{v}_{coll}^i]^2/2\sigma_i^2)$ with three independent principal axes to approximate the situation before breakup. We then assume that

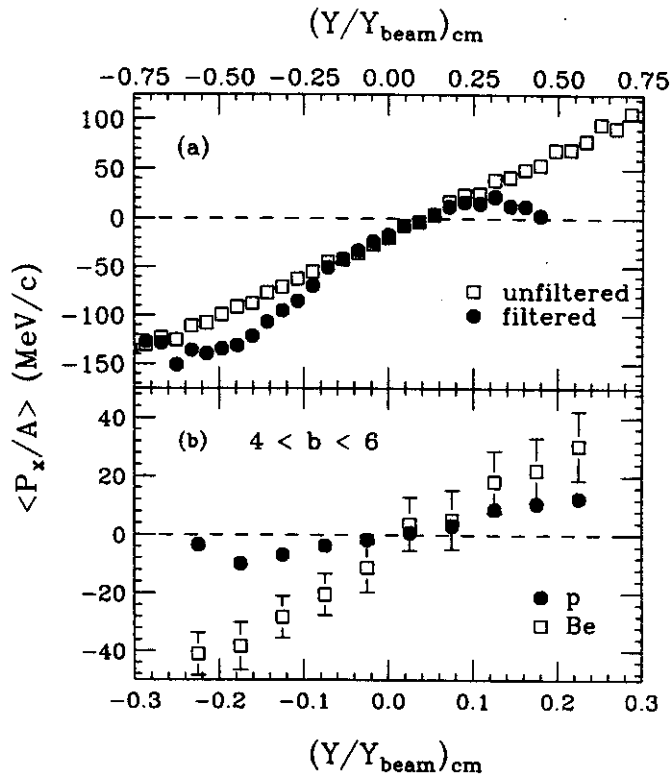

Figure 1: (a) Simulations for the transverse momenta of α particles with the thermal model of Eq. 3. Open and filled circles depict calculations with the model before and after corrections for the experimental acceptance have been applied. (b) Mean transverse momenta measured for p and Be fragments at 4<b<6 fm.

the momenta of the produced particles obtain additional random velocity components according to the distribution $\mathcal{G}(v_{ih}) \propto exp(-Av_{ih}^2/2T)$, where A is the fragment mass number and T is a temperature parameter. The principal axes of the collective velocity distribution are rotated by the flow angle, θ_F; σ_3 characterizes the distribution along the flow axis and σ_1 and σ_2 characterizes the other widths in and perpendicular to the reaction plane, respectively. These widths were adjusted to reproduce the measured rapidity and transverse energy distributions. The solid line in Fig. 2, for calculations assuming $\sigma_1 = 0.1c, \sigma_2 = 0.1c, \sigma_3 = 0.16c, \theta_F = 40°$, and $T = 45$ MeV, reproduces the main experimental trends. While this parameterization is not unique, the observed constancy of the heavy fragment flow can only be reproduced if it is primarily governed by the collective velocity distribution. The flow for light particles is then reduced relative to that for heavy fragments due to thermal mixing between the collective velocity distributions at positive and negative rapidities in the c.m. system.

Since coalescence and thermodynamic models make equivalent predictions in the limit of local thermal equilibrium [14], the agreement between the measured and calculated mass dependence can be regarded as a partial justification for the utilization of cluster production mechanisms [15] that have similarities to the coalescence approximation. For comparisons to the proton flow predicted by transport models such as the Boltzmann-Uehling-Uhlenbeck (BUU) equation, we have taken advantage of this observation to construct an effective proton flow

$$F_{eff} = \sum Z_i Y_i F_i / \sum Z_i Y_i, \tag{4}$$

where the Z_i, Y_i, and F_i are the charge, yield, and flow values for the various particle species. In Fig. 3

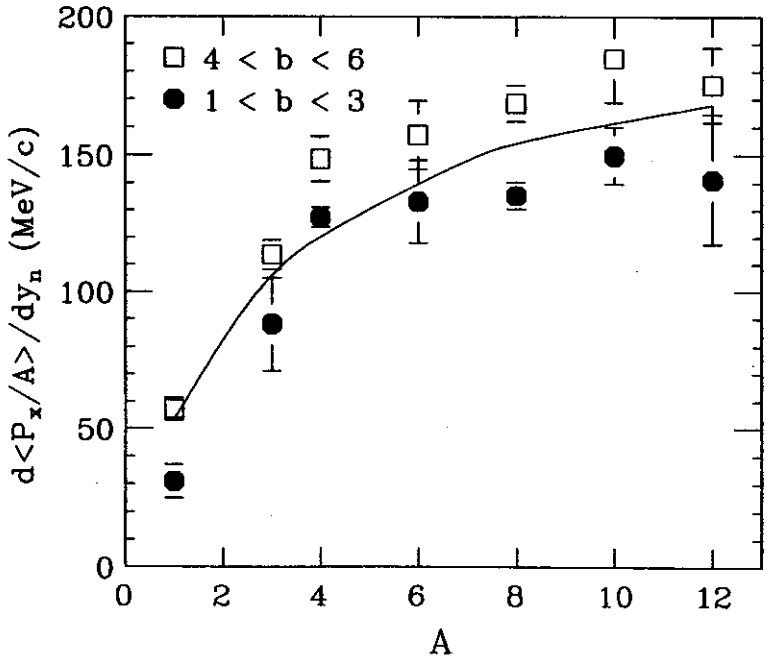

Figure 2: The mass dependence of the collective sidewards flow per nucleon in the reaction plane, $d\langle p_x/A\rangle/dy_n$ for the two impact parameter gates used in the analysis. Here we assume A=2Z for A> 4, where mass identification was not achieved. The solid line shows a calculation with the thermal model of Eq.3.

the experimental effective proton flow is plotted against impact parameter as the solid points. The width of the horizontal bars represents the relevant impact parameter bin.

To test the sensitivity of this measurement to the transport parameters, BUU calculations have been performed for various parameterizations of the mean field potential and including a nucleon-nucleon cross section which has been parameterized to describe measured nucleon-nucleon scattering data [16]. These calculations are shown in Fig. 3 for a soft (K=200 MeV) mean field (SM - small triangles) and a hard (K=386 MeV) mean field (HM - large triangles) with a momentum dependence consistent with non-locality effects observed in nucleon-nucleus potential scattering [17]. Calculations with a soft mean field (S - open squares) and a hard mean field (H - open circles) without momentum dependence are also shown. All calculations have been impact parameter averaged and filtered by the experimental acceptance.

The qualitative trends of the data are much better described by momentum dependent mean fields. The degeneracy between calculations with soft momentum dependent and hard momentum independent mean fields, observed for symmetric Nb+Nb or La+La [18,19,20] systems, is broken for this mass asymmetric system, consistent with the observations of ref. [20]. The sensitivity to the compressibility parameter K is slight, however. Consistent with the systematics of the disappearance of collective flow [21] and with microscopic calculations of the in-medium corrections to the nucleon-nucleon cross section [22], improved agreement between the momentum dependent calculations and the data can be obtained by a 20% density dependent reduction of the in-medium nucleon-nucleon cross section of the form $\sigma_{NN} = (1 - 0.2\frac{\rho}{\rho_o})\sigma_{free}$ [21], This is illustrated by the solid points in the Fig. 3 for a soft momentum dependent mean field (SM $(0.8\sigma_{free})$).

a. Laboratoire National SATURNE, CEN Saclay, 91191 Gif-sur-Yvette Cedex, France
b. Department of Chemistry, Washington University, St. Louis, MO 63130
c. Gesellschaft für Schwerionenforschung, D-6100 Darmstadt 11, Germany
d. IUCF and Department of Chemistry, Indiana University, Bloomington, IN 47405
e. Instituto de Fisica, Universidade de São Paulo, CEP 01498, São Paulo, Brazil

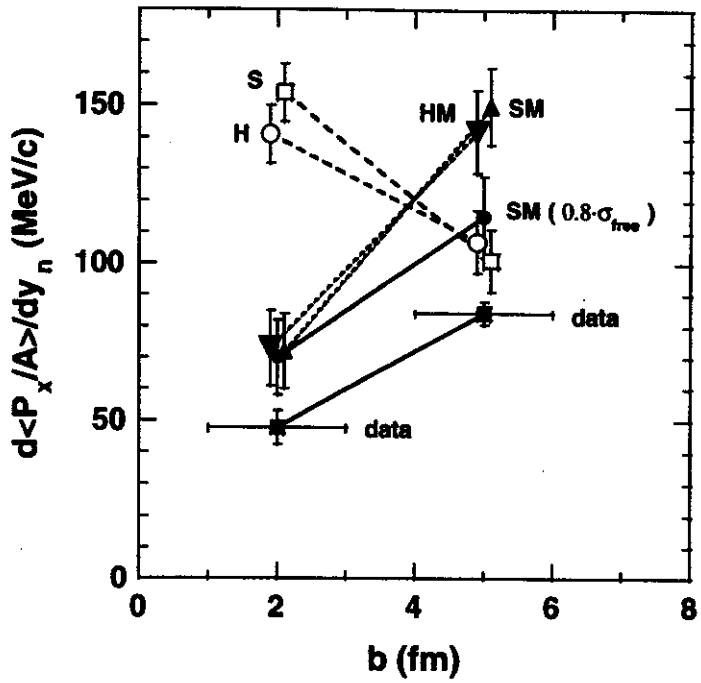

Figure 3: The solid square points with horizontal error bars depict the measured effective proton flow. Also shown are the corresponding BUU calculations for the following parameter sets: **H** - hard EOS without momentum dependence (open circles), **S** - soft EOS without momentum dependence (open squares), **HM** - hard EOS with momentum dependence (large triangles), **SM** - soft EOS with momentum dependence (small triangles). **SM** ($0.8\sigma_{free}$) - soft EOS with momentum dependence and a 20% reduction in the nucleon-nucleon cross-section (solid circles). The theoretical error bars are purely statistical.

References

1. H.H. Gutbrod, A.M. Poskanzer and H.G. Ritter, Rep. Prog. Phys., 52, 1267 (1989) and refs. therein.
2. H. Stöcker and W. Greiner, Phys. Rep., 137, 277 (1986) and refs. therein.
3. M.D. Partlan *et al.*, Phys. Rev. Lett. 75, 2100 (1995).
4. K.G.R. Doss *et al.*, Phys. Rev. Lett. 59, 2720 (1986).
5. G. Peaslee *et al.*, Phys. Rev. C 49, R2271 (1994).
6. M. B. Tsang et al., Phys. Rev. Lett. 71, 1502 (1993).
7. R.T. de Souza et al, Nucl.Instr.Meth.A 295,109(1990); The Miniwall, a granular extension of the Miniball to forward angles, uses the readout technology of D.W. Stracener et al, Nucl.Inst.Meth.A 294,485(1990).
8. P. Danielewicz and G. Odyniec, Phys. Lett.157B, 146 (1985).
9. Here, the reaction plane is defined to be perpendicular to the total angular momentum.
10. J.P. Sullivan and J. Péter, Nucl. Phys. A540, 275 (1992).
11. P. Danielewicz *et al.*, Phys. Rev. C 38, 120 (1988).
12. This ratio was of order 0.3, but varied with impact parameter [5]. Recoil corrections are small.
13. S. Wang *et al.*, Phys. Rev. Lett. 74, 2646 (1995).
14. L.P. Csernai and J.I. Kapusta, Phys. Rep. 131, 223 (1986) and refs. therein.
15. P. Danielewicz and G.F. Bertsch, Nucl. Phys. A533, 712 (1991).
16. D. Klakow, G. Welke, and W. Bauer, Phys. Rev. C48, 1982 (1993).
17. C. Gale et. al., Phys. Rev. C41, 1545 (1990).
18. C. Gale et al., Phys. Rev. C35, 1666 (1987).
19. J. Aichelin et al., Phys. Rev. Lett. 58, 1926 (1987).
20. Q. Pan and P. Danielewicz, Phys. Rev. Lett. 70, 2062, 3523 (1993).
21. G.D. Westfall et al., Phys. Rev. Lett. 71, 1986 (1993).
22. T. Alm, Nucl. Phys. A587, 815 (1995).

RADIAL FLOW IN INTERMEDIATE ENERGY HEAVY-ION COLLISIONS

R. Pak, D. Craig,[a] E. E. Gualtieri, S. A. Hannuschke, R. A. Lacey,[b] J. Lauret,[b]
W. J. Llope,[c] N. T. B. Stone, A. M. Vander Molen, G. D. Westfall, and J. Yee

Collective motion of nucleons in heavy-ion collisions offers a glimpse at the true many-body effects not present in simple superpositions of individual two-body interactions. Derivation of an equation of state (EOS) for nuclear matter has been the main motivation for studying the collective effects resulting from these collisions. Collective radial expansion of particle emission from central nuclear collisions, termed radial flow, was originally postulated to explain the observed differences in the slopes of the inclusive pion and proton energy spectra [1]. Radial flow was primarily attributed to the conversion of thermal and compressional energy into work through a pressure gradient in the hydrodynamic limit [1,2]. Consequently, the fragments acquire a net outward radial velocity in addition to their random thermal component, which is evident from the increased curvature in the single-particle energy spectrum. After directed collective transverse flow was demonstrated to be a signature of hydrodynamical compression [3], a study of transverse energy production [4] was undertaken, aimed at accounting for the discrepancy between the measured and calculated thermal mean transverse energies. In that investigation, approximately 40% of the total kinetic energy in the center-of-mass (c.m.) frame was reported to be converted into compressional energy in the moment of highest density [4].

Subsequent work [5,6,7,8,9,10] for heavy systems at relatively high beam energies ($\gtrsim$ 100 MeV/nucleon) has also revealed that radial flow is a major contribution to the energy dissipation in the disassembly process of excited nuclear matter. Indications are that radial flow also persists down into the intermediate beam energy regime [11,12,13,14,15]. We present results from a systematic study for the incident beam energy and impact parameter dependence of collective radial flow for a relatively light system in this energy regime. Comparison to predictions of Boltzmann-Uehling-Uhlenbeck (BUU) model and WIX multifragmentation model calculations showing agreement with our measured values of radial flow observables are presented. We shall show that the relative contribution of collective radial flow extracted from the mean transverse kinetic energy accounts for approximately half of the emitted particle's energy for the heavier fragments ($Z \geq 4$) at the highest beam energy studied here.

The present measurements were carried out with the Michigan State University 4π Array [16] at the National Superconducting Cyclotron Laboratory (NSCL) using beams from the K1200 cyclotron. A target of 1.0 mg/cm^2 Sc was bombarded with ^{40}Ar projectiles ranging in energy between 35 and 115 MeV/nucleon in 10 MeV/nucleon steps. Beam intensities were approximately 100 electrical pA. Prior to this experiment, the MSU 4π Array was upgraded with the High Rate Array (HRA). The HRA is a close-packed pentagonal configuration of 45 phoswich detectors spanning polar angles $3° \lesssim \theta_{lab} \lesssim 18°$. With the HRA we obtained Z resolution up to the charge of the ^{40}Ar projectile, and mass resolution for the hydrogen isotopes. The main ball of the 4π Array consists of 55 Bragg curve counters followed by 170 phoswich detectors covering the angles $18° \lesssim \theta_{lab} \lesssim 162°$. Data were taken with a minimum bias trigger that required at least one hit in the HRA (HRA-1 data), and a more central trigger where at least two hits in the main ball (Ball-2 data) were required. The radial flow analysis described below was performed with the Ball-2 data.

The importance of selecting central events to search for a radial flow signal has been emphasized [6,8,10,11,13] because stopping power, compression, and equilibration are expected to be greatest for

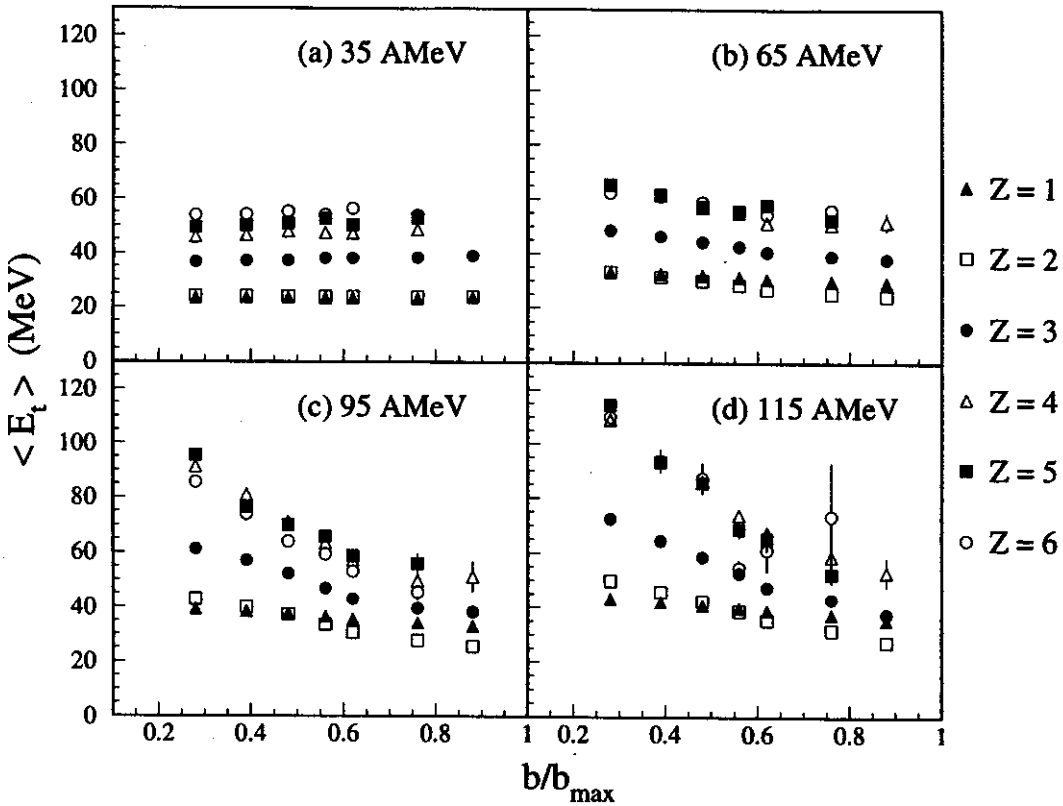

Figure 1: Mean transverse kinetic energy of fragments from ^{40}Ar+^{45}Sc reactions at polar angles $\theta_{\rm c.m.} = 90° \pm 15°$ versus the reduced impact parameter at four incident beam energies.

collisions at small impact parameters. We assign the impact parameter b of each event through cuts on centrality variables [17] measured with the improved acceptance of the upgraded MSU 4π Array. The centrality variable chosen for the present analysis was the midrapidity charge of each event Z_{mr}. Using methods similar to those detailed elsewhere [18], Z_{mr} is found to be an appropriate variable to use as a centrality filter for this system over the range of beam energies studied, and does not autocorrelate with the radial flow observables. Events with larger Z_{mr} correspond to events with smaller impact parameters. Details of our method for impact parameter selection used in the analysis below are given elsewhere [19].

In addition to selecting central collisions to search for a radial flow signal, reaction products should be measured at 90° in the center-of-mass (c.m.) frame in order to suppress the contamination by spectator emission and directed flow effects [1,5,7,10]. We present in Figure 1 the mean transverse kinetic energy $\langle E_t \rangle$ for six different particle types plotted versus the reduced impact parameter $\hat{b} = (b/b_{max})$ at four incident beam energies. The data are for ^{40}Ar+^{45}Sc reactions at $\theta_{\rm c.m.} = 90° \pm 15°$, and the errors shown are statistical. Up to a projectile energy of 55 MeV/nucleon the data exhibit a constant value of $\langle E_t \rangle$ for each particle type, while above 55 MeV/nucleon a monotonic rise in the values of $\langle E_t \rangle$ occurs as the impact parameter becomes smaller. At the higher beam energies, where detector low-energy thresholds have a less significant effect, the dramatic increase in the values of $\langle E_t \rangle$ for the heavier fragments produced in central collisions is linked to larger values of the radial flow energy. This is in contrast to expectations of a purely thermal source for which the different particle types are emitted with the same mean kinetic energy. This result is in qualitative agreement with previous data [4] and transport model calculations [5], which attributed this phenomenon to collective expansion of a blast of light fragments from central

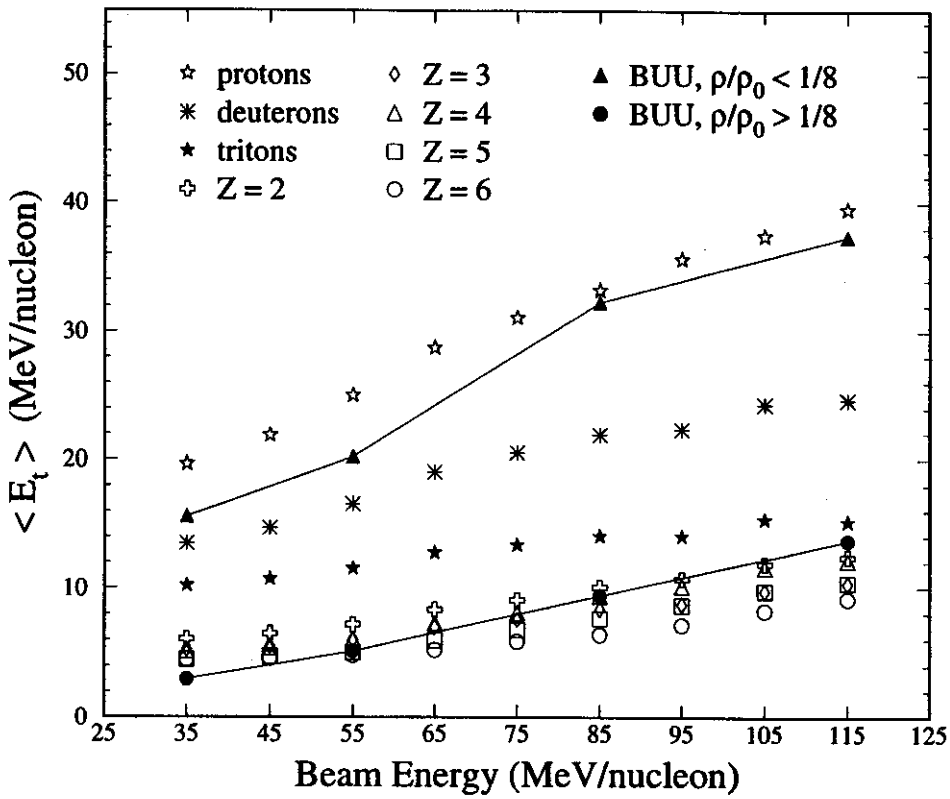

Figure 2: Mean transverse kinetic energy per nucleon of fragments from central ^{40}Ar+^{45}Sc collisions at polar angles $\theta_{\mathrm{c.m.}} = 90° \pm 15°$ versus incident beam energy compared with predictions of BUU model [13] calculations. The lines are included to guide the eye.

collisions.

To estimate the magnitude of the mean transverse kinetic energy imparted to the fragments in the nuclear disassembly process, we used a Boltzmann-Uehling-Uhlenbeck (BUU) model calculation [13]. The calculations were performed at a fixed impact parameter of b = 0 for an EOS with compressibility κ = 240 MeV, and were not corrected for effects due to detector acceptance. We show in Figure 2 measured excitation functions of $\langle E_t \rangle$ per nucleon compared to the predictions of the BUU model calculations. The solid triangles in this figure are the maximum values of $\langle E_t \rangle$ at the respective incident beam energies for the case where only particles in medium with density $\rho/\rho_0 < \frac{1}{8}$ are included in the calculation. For particles in medium with $\rho/\rho_0 < \frac{1}{8}$, we found collisions are no longer sufficiently frequent to allow conversion of thermal and compressional energy into collective radial flow. There is surprising agreement between these points and the data for the protons (open stars). To extract the maximum values of $\langle E_t \rangle$ for the case where only particles in medium with $\rho/\rho_0 > \frac{1}{8}$ are considered, we must first subtract out two thirds of the value of the Fermi energy for the initial configuration before the collision. These values, plotted as solid circles in Figure 2, show good agreement with the data for fragments with $Z \geq 2$. Although our BUU calculations involve only nucleons, we are still able to delineate the approximate limits on the value of $\langle E_t \rangle$ as a function of incident beam energy reasonably well.

We have simulated collective radial expansion of light fragment emission in heavy-ion collisions using the statistical multifragmentation model called WIX [20]. The WIX code generated events in which a single source de-excites via explosion and evaporation with this specified collective expansion

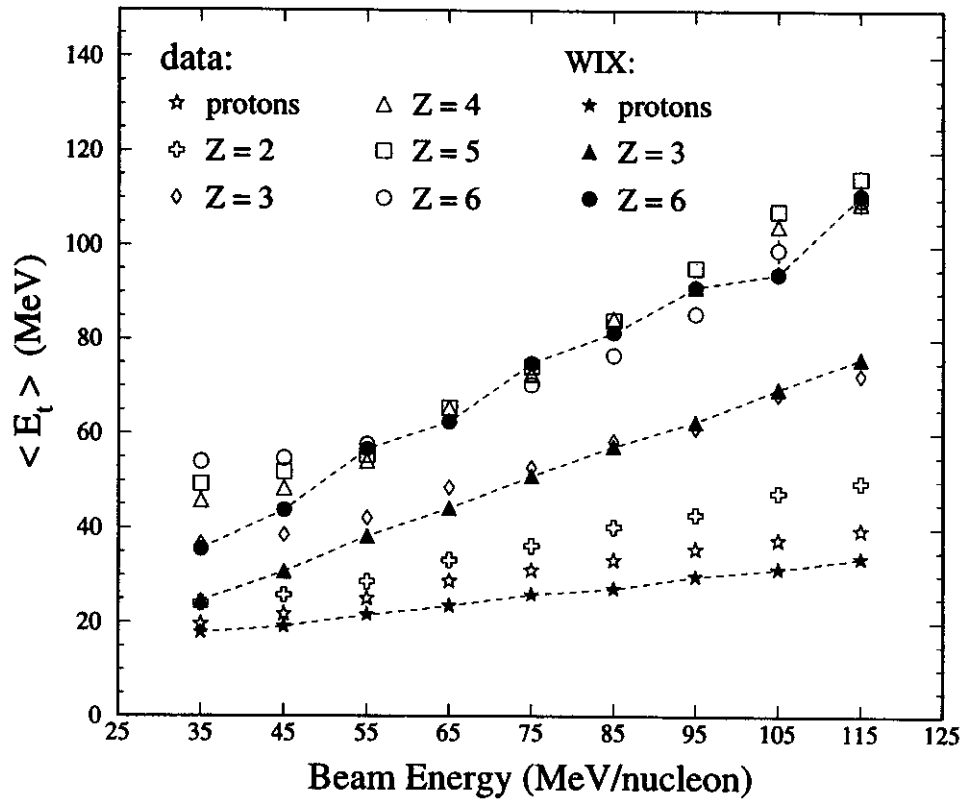

Figure 3: Mean transverse kinetic energy of fragments from central ^{40}Ar+^{45}Sc reactions at polar angles $\theta_{c.m.} = 90° \pm 15°$ versus incident beam energy compared with predictions of WIX model [20] calculations assuming half the available energy is associated with radial flow. The lines are included to guide the eye.

energy at freeze-out. The calculations included the Coulomb interaction between fragments, and the default parameters were used to characterize the level density, explosion threshold energy, and spacial configuration of the decaying source. The simulated events were analyzed with the same radial flow routine as for the actual data. In Figure 3 we show a comparison between data and simulation for the excitation functions of the mean transverse kinetic energy for various light fragment types. The open symbols are data from central ^{40}Ar+^{45}Sc reactions at polar angles $\theta_{c.m.} = 90° \pm 15°$. The solid symbols are the predictions of the WIX multifragmentation model assuming half the available energy of the disassembly process is associated with radial flow. All effects of the experimental acceptance were included in these filtered simulations. The errors shown are statistical, and the dashed lines are included only to guide the eye. Similar trends are present in the filtered simulation of the other particle types not shown for clarity. The agreement between data and simulation in Figure 3 demonstrates that the measured radial flow is not an artifact of our detector acceptance or analysis method, and substantiates our claim that approximately half of the emitted particle's energy originates from collective radial expansion [21].

In summary, we have investigated collective radial flow of light fragments from ^{40}Ar+^{45}Sc reactions at beam energies in the range E = (35 - 115) MeV/nucleon using the MSU 4π Array upgraded with the HRA. Collective radial flow of light fragments in the nuclear disassembly process was demonstrated through transverse energy production. The mean transverse kinetic energy of the different fragment types increases with event centrality, and increases as a function of the incident beam energy. At the higher beam energies, the dramatic increase in the values of $\langle E_t \rangle$ for the heavier fragments produced in central

collisions is linked to larger values of the radial flow energy. This is in contrast to expectations of a purely thermal source for which the different particle types are emitted with the same mean kinetic energy. Comparison of our measured values of $\langle E_t \rangle$ shows agreement with predictions of BUU model and WIX multifragmentation model calculations. The radial flow extracted from $\langle E_t \rangle$ accounts for approximately half of the emitted particle's energy for the heavier fragments ($Z \geq 4$) at the highest beam energy studied.

a. Department of Physics, University of Wisconsin, Madison, WI 53706.
b. Department of Chemistry, SUNY - Stony Brook, Stony Brook, NY 11794.
c. T. W. Bonner Nuclear Laboratory, Rice University, Houston, TX 77251.

References

1. P. J. Siemens and J. O. Rasmussen, Phys. Rev. Lett. 42, 880 (1979).
2. J. P. Bondorf, S. I. A. Garpman, and J. Zimanyi, Nucl. Phys. A296, 320 (1978).
3. H. A. Gustafsson *et al.*, Phys. Rev. Lett. 52, 1590 (1984).
4. K. G. R. Doss *et al.*, Mod. Phys. Lett. A 3, 849 (1988).
5. P. Danielewicz and Q. Pan, Phys. Rev. C 46, 2002 (1992).
6. S. C. Jeong *et al.*, Phys. Rev. Lett. 72, 3468 (1994).
7. W. C. Hsi *et al.*, Phys. Rev. Lett. 73, 3367 (1994).
8. P. Danielewicz, Phys. Rev. C 51, 716 (1995).
9. G. Poggi *et al.*, Nucl. Phys. A586, 755 (1995).
10. M. A. Lisa *et al.*, Phys. Rev. Lett. 72, 2662 (1995).
11. H. W. Barz *et al.*, Nucl. Phys. A531, 453 (1991).
12. R. T. de Souza *et al.*, Phys. Lett. B 300, 29 (1993).
13. W. Bauer *et al.*, Phys. Rev. C 47, R1838 (1993).
14. D. Heuer *et al.*, Phys. Rev. C 50, 1943 (1994).
15. F. Schussler *et al.*, Nucl. Phys. A584, 704 (1995).
16. G. D. Westfall *et al.*, Nucl. Inst. and Methods A238, 347 (1985).
17. C. Cavata *et al.*, Phys. Rev. C 42, 1760 (1990).
18. W. J. Llope *et al.*, Phys. Rev. C 51, 1325 (1995).
19. R. Pak *et al.*, Phys. Rev. C 53, R1469 (1996).
20. J. Randrup, Comp. Phys. Comm. 77, 153 (1993).
21. R. Pak *et al.*, submitted to Phys. Rev. C.

MULTISTEP SCATTERING IN THE 160 MEV ^{208}Pb(α,α') REACTION

M. Thoennessen, E. Ramakrishnan[a], T. Baumann[b], A. Azhari, R. A. Kryger, R. Pfaff, S. Yokoyama, J. R. Beene[c], M. L. Halbert[c], P. E. Mueller[c], G. van Buren[d], R. J. Charity[d], P-F. Hua[d], D. G. Sarantites[d], L. G. Sobotka[d], M. B. Chadwick[e], and M. Hussein[f]

Heavy- and light-ion inelastic scattering has been extensively used to investigate giant resonances [1] built on the ground state. It was suggested a few years ago that inelastic heavy-ion scattering can also be applied in order to study the decay of the giant dipole resonance (GDR) built on highly excited states [2]. The GDR built on excited states had been measured predominantly with fusion evaporation reaction [3]. This new method of exciting a compound nucleus by inelastic scattering provided an opportunity to measure the GDR strength function as a function of excitation energy, and independent of angular momentum, since small angle scattering populates predominantly low angular momentum states. The main assumption to be fulfilled is a rapid equilibration of the target nucleus so that the decay can be described with a statistical model. Although it has been shown that this assumption is fulfilled up to at least 45-50 MeV [2] it is necessary to understand the production mechanism for these excited states of the target nucleus.

In a recent experiment we measured high energy γ-rays (5 - 30 MeV) in coincidence with inelastically scattered α particles following the reaction ^{208}Pb(α,α') at E_α = 160 MeV. The excitation energy of the excited ^{208}Pb was derived from the energy loss of the scattered α-particle and the excitation energy dependence of the GDR width was extracted [4]. Simultaneously, α singles spectra which yielded the initial population distribution of the excited ^{208}Pb, were recorded. Details of the experimental setup are provided in Ref. [4]. In the present paper we will concentrate on the analysis of the α singles spectra in order to investigate and explain the production mechanisms. We will apply the quantum mechanical preequilibrium multistep scattering theory of Feshbach, Kerman and Koonin (FKK) [5].

The continuum emission of α particles emitted in (α,α') reactions can be understood in terms of the preequilibrium emission of α particles following the interaction of the projectile α particle with one, or more, nucleons in the target nucleus. Such inelastic scattering processes occur in competition with other mechanisms such as the break-up of the α particle into individual nucleons in the field of the nucleus. Gadioli *et al.* [6] have analyzed many of the possible reaction mechanisms for the interaction of an α particle with a nucleus, using the semiclassical exciton model. In the case of inelastic (α,α') reactions they assumed a preequilibrium reaction mechanism in which the α particle excites nucleon particle-hole pairs, and successfully accounted for a number of inclusive continuum α emission spectra. In this work we use the FKK theory to evaluate such processes. One of the main advantages of the FKK theory is that it predicts double- differential spectra, not just angle-integrated spectra, and automatically includes quantum effects such as diffraction, refraction, and finite-size effects of the α particle in the nuclear and coulomb nuclear field, which are known to be important in determining angular distributions [7].

Most calculations using the FKK theory have been for nucleon-induced reactions. The FKK theory calculated the multistep direct (MSD) scattering contributions as a convolution of one-step scatterings. To modify the formalism for α projectiles is straightforward since the basic equations for multistep direct reactions are unchanged and one has only to replace the unbound nucleon distorted waves with α particle distorted waves in the DWBA matrix elements [8]. One additional modification is the inclusion of an α particle survival factor S. This is a reduction factor accounting for the fact that during the scattering of the

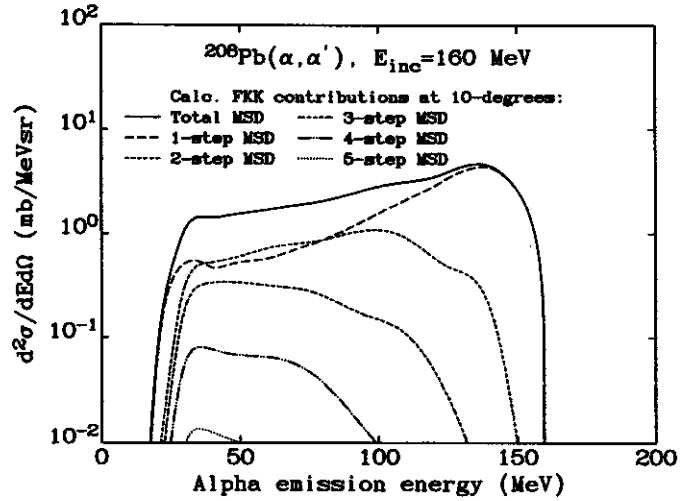

Figure 1: Calculated multistep direct (MSD) contributions in ^{208}Pb(α, α') inelastic scattering, at 10°.

α particle with a nucleon, the α particle may instead undergo fragmentation. It is difficult to determine S accurately; we use Gadioli's estimate of $S = 2/3$, based on the ratio of experimental free inelastic to elastic α-nucleon cross sections [6,9].

In Figure 1 the various multistep contributions which make up the full preequilibrium inclusive α-emission spectrum at 10° are shown. 1-step scattering processes are dominant at the higher emission energies. This is to be expected since multistep scatterings tend to result in a larger energy-transfer to the residual nucleus (there are more particle-hole states created), and also tend to result in a scattering to wider angles (more collisions broaden the angular distribution). At the lower emission energies it is evident that two- and three-step scattering is comparable in magnitude to 1-step scattering. Since the energy-loss here is rather large, the probability of two or three collisions of the α projectile with bound nucleons prior to emission is fairly high. The general shape of the calculated emission spectrum is qualitatively similar to that found for nucleon-induced reactions at the same energy [10]. The sharp decrease in the calculated spectrum in the energy range 20-30 MeV is due to the effect of the Coulomb barrier. Figure 1 shows that multistep scatterings beyond three steps do not contribute significantly to the spectrum. This is, however, partly due to the fact that the results are for scattering in the forward-direction, and if one considers back-angle emission the four- and five- step scattering contributions become important for large energy-loss processes.

Figure 2 compares our experimental data (at angles between 10°– 20°) with the calculated α spectrum at 10°, which includes both the preequilibrium mechanism and α particles emitted through compound nucleus equilibrium decay. The data at the very highest emission energies are from elastic scattering, and are not included in this analysis. It is evident that the calculations account for the general features of the experimental data rather well: the "hard tail" can be explained by the preequilibrium emission, and the rise at the lowest energy by evaporation. However, it is also evident that just above the evaporation regime, for emission energies between approximately 30 and 50 MeV, the calculated mechanisms underpredict the data. At these emission energies the compound nucleus decay cross sections are too small to be able to explain this deficiency, due to the low density of states in the residual nuclei.

Our neglect of other nuclear reaction mechanisms may be responsible for the calculated shortfall in the cross section between 30 and 50 MeV. Possible mechanisms which may be contribute are: (1)

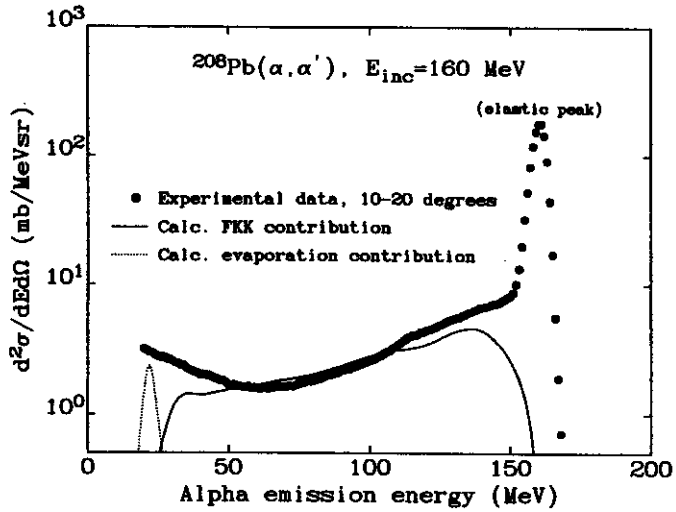

Figure 2: Comparison of calculated ^{208}Pb(α, α') inelastic scattering with experimental data. Elastic scattering is not included in the calculation.

quasi-elastic scattering of the α-particle projectile with a preformed α particle within the nucleus, both α particles being emitted [6]; (2) α particles being emitted in a four-nucleon coalescence process, after the initial fragmentation of the α projectile; (3) knockout of a preformed α particle following previous inelastic scatterings. To summarize, this is the first FKK analysis of (α, α') reactions, and our results accounts for many features of the measured data, but there is evidence that other mechanisms (described above) may also contribute. Numerical calculations of these additional mechanisms are in progress.

a. Present address: Cyclotron Laboratory, Texas A&M University, College Station, TX 77843.
b. Present address: Gesellschaft für Schwerionenforschung, D-64220 Darmstadt, Germany.
c. Oak Ridge National Laboratory, Operated by Lockheed Martin Energy Res. Oak Ridge, TN 37831.
d. Department of Chemistry, Washington University, St. Louis, MO 63130.
e. Lawrence Livermore National Laboratory, Nuclear Data Group, Livermore, CA 94550.
f. Instituto de Fisica, Universidade de Sao Paulo, Caixa Posta 02139, 01498 Sao Paulo, S.P., Brazil.

References

1. *Proceedings of the Gull Lake Nuclear Physics Conference on Giant Resonances*, Nucl. Phys. A569 (1994), and *Proceedings of the Groningen Conference on Giant Resonances*, Nucl. Phys. A, in press (1996).
2. M. Thoennessen, *et al.* Phys. Rev. C 43, R12 (1991).
3. K. A. Snover, Ann. Rev. Nucl. Part. Sci. 36, 545 (1986), J. J. Gaardhøje, Ann. Rev. Nuc. Part. Sci., 42, 483 (1992).
4. E. Ramakrishnan *et al.*, *Proceedings of the Groningen Conference on Giant Resonances*, Nucl. Phys. A, in press (1996), E. Ramakrishnan *et al.*, submitted to Phys. Lett. B (1996).
5. H. Feshbach. A.K. Kerman, S. Koonin, Ann. Phys. (N.Y.) 125, 429 (1980).
6. E. Gadioli, E. Gadioli Erba, J. J. Hogan, and B. V. Jacak, Phys. Rev. C 29, 76 (1984); E. Gadioli and E. Gadioli Erba, Z. Phys. A 299, 1 (1981); E. Gadioli, E. Gadioli Erba, J. J. Hogan, and K. I. Burns, Z. Phys. A301, 289 (1981).
7. M. Blann, W. Scobel, and E. Plechaty, Phys. Rev. C 30, 1493 (1984).
8. M. B. Chadwick *et al.*, *Proc. of the First Latinamerican Workshop on: On and Off Beam Gamma Spectroscopy for the Study of Heavy Ion Reaction and Pre-equilibrium Processes*, September 4-8, 1995, Caracas, Venezuela, to be published in Heavy Ion Physics (1996).
9. E. Gadioli and P. E. Hodgson, Pre-Equilibrium Nuclear Reactions, Clarendon Press, Oxford (1992); see particularly pages 417-435.
10. M. B. Chadwick, P. G. Young, D. C. George, and Y. Watanabe, Phys. Rev. C 50, 996 (1994).

SEARCH FOR THE DECAY OF NON-COMPACT GEOMETRIES

N.T.B. Stone, G.D. Westfall, E.E. Gualtieri, S.A. Hannuschke, R. Lacey,[a] J. Lauret,[a] W.J. Llope,[b]
R. Pak, O. Bjarki, A.M. Vander Molen, and J. Yee

1. INTRODUCTION

Recent theoretical calculations have raised one of the most intriguing questions today in intermediate energy nuclear physics. This question concerns the formation of exotic shapes in nuclear matter. There have been many theorists, using a rich diversity of models to simulate nuclear dynamics, who have predicted the occurrence of such shapes.[1,2,3,4,5] The title "non-compact geometries" refers to the position-space distribution of the nucleons of a combined nuclear system shortly after a nucleus-nucleus collision, and implies short-lived configurations with novel shapes, *e.g.* toroids or bubbles. A solid sphere is the geometrical configuration with the minimum surface area for a given volume, *i.e.*, the most compact shape. In this light, any shape other than a sphere can be called "non-compact."

In some model predictions, the formation of these geometries follows a simple progression, beginning with the target and projectile colliding, and including dynamic developments like the propagation of shock waves through the combined system, or perhaps a compression and subsequent radial expansion.[1] One consequence of such a radial expansion could be the formation of a bubble-like geometry.

Other predictions describe a contraction of the system along the beam axis, effectively converting an initially spherical shape to a more oblate, "pancake" shape.[2] Such a contraction along the beam axis would be caused by the initial parallel momentum of the projectile and target combination. This contraction could give rise to a disk-like geometry.

Still other alternative explanations of the formation of these shapes invoke a dynamic, mechanical or "spinodal" instability of the combined system, which fragments the system after the ensuing compression and expansion.[6] The non-compact essence in this process occurs via the interference of compression waves propagating within the combined nucleus.

Thus, as one can see, the predicted origins of these unusual geometries are diverse and sometimes exotic in and of themselves. What is common to all such predictions is that there are expected consequences of the formation of all such geometries. With most of these predictions, theorists have described experimental observables which should be sensitive, in some way, to the formation of these shapes. There are several such observables predicted to show some specific change in behavior, beyond simple systematic trends, that may be attributed to the formation of these unique geometries. These "signatures" can be sought out, analyzed, and cataloged to support or refute theoretical claims of the existence of these unique geometries.

The goal in this study is to analyze these observables, in systems where these geometries are formed, and look for the predicted signatures of formation. Some recent studies have focused on aspects of the formation and detection of these geometries,[7,8,9] but this study will examine both experimental signatures and their systematic trends, spanning a large excitation function.

2. SIGNATURES

The experimental data for this study were collected for the ^{86}Kr+^{93}Nb system for incident beam energies ranging from 35 to 95 AMeV with the MSU 4π Array.[10] Only central events will be considered in

this analysis, since these geometries, if they are formed, are predicted for central collisions. We will select these events from the inclusive data sets using the widely-practiced method of "centrality variables,"[11] so called because their values have been shown to be correlated to the impact parameter of the collision. Some examples are the number of observed charged particles (N_c), the total transverse kinetic energy (E_t), and the total charge of particles at mid-rapidity (Z_{mr}). By selecting only events characterized by a value of a given centrality variable which falls within a given range, one thus constrains the value of the impact parameter for these events.

The first signature we present is the sphericity (S) of particle emission. Sphericity[12] is defined by first generating the kinetic energy tensor such that $T_{ij} = \sum_{n=1}^{N_{imf}} \frac{p_{i,n}p_{j,n}}{2m_n}$, where N_{imf} is just the number of Intermediate-Mass Fragments (IMFs, particles with $3 \leq Z \lesssim 20$) in each event, and $p_{i,n}$ and m_n are the i^{th} component of the momentum and the mass of each particle, respectively. Next, one calculates the eigenvalues (λ_i) of this tensor, which correspond to the sizes of the axes of the ellipsoid in momentum space. These eigenvalues are then ordered ($\lambda_1 > \lambda_2 > \lambda_3$) and normalized ($q_i = \lambda_i^2 / \sum_{j=1}^{3} \lambda_j^2$), and the sphericity is defined as $S = \frac{3}{2}(q_2 + q_3)$. Given this definition, events with isotropic emission of fragments will have a high value of sphericity, while those with co-planar, rod-like, or otherwise non-spherical emission will have lower values.

The sphericity is expected to exhibit sensitivity particularly to the occurrence of the co-planar geometries.[3] To be specific, once the nucleons are distributed in a co-planar configuration, there is very little Coulomb repulsion along the beam axis, and, since the remaining forces direct the emission of fragments away from the center, this leaves the fragments moving outward in their plane of formation. This overall direction of emission is precisely what is measured by the sphericity. The consideration of only intermediate-mass fragments is expected to enhance the sensitivity of the experimental signatures.

We have calculated the mean values of the sphericity ($\langle S \rangle$) of IMF emission in central events, selected via 5% cuts on Z_{mr}, and plotted these versus the incident beam energy for three representative IMF multiplicities (Fig. 1). In fact, this range of multiplicities ($3 \leq Z \leq 7$) accounts for roughly 90% of the central events for all beam energies above 35 AMeV. To give greater meaning to the absolute values of $\langle S \rangle$, we have plotted, above and below each of these three, the resulting mean values obtained from a model[13] which produced spherical and disk-like events. The separation between each of these three sets of values is a result of the multiplicity dependence of the observable itself. This must be explicitly treated, and has been understood since the conception of sphericity.[12]

What we see in this figure is that, for low incident energies, the experimental data yield values of $\langle S \rangle$ similar to those found for the spherical simulation, indicating spherical emission of IMFs. As the energy increases, however, the data exhibit a striking suppression in the value of $\langle S \rangle$ at an incident beam energy of 60 AMeV. This indicates more disk-like or coplanar IMF emission at this energy, particularly for the higher IMF multiplicities. As the energy continues to increase, the experimental IMF emission returns to a more spherical pattern, with some slight systematic decrease in the mean value near the highest energies. It is precisely this appearance of the suppression of the sphericity of IMF emission, and subsequent disappearance, that is a signature of non-compact geometry formation.[3]

The second and third signatures we now present are the number of IMFs (N_{IMF}) and the total charge of all detected IMFs (Z_{IMF}). These observables are also expected to show sensitivity to the occurrence of non-compact geometries.[1,3] To explain, let us consider again the dynamics of the collision. As the combined nuclear system expands, the density decreases and the system cools. This expansion, which may result in a brief stall, is expected to cool to lower nuclear temperatures than other more rapid

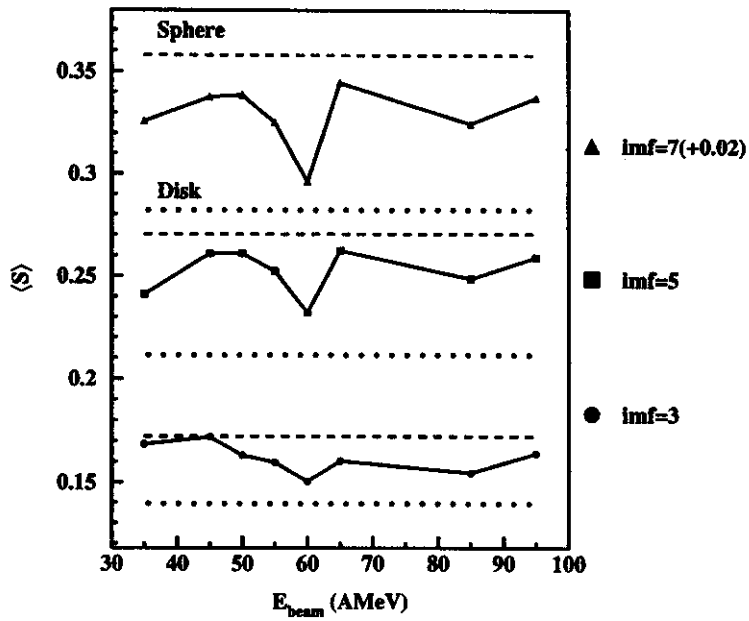

Figure 1: $\langle S \rangle$ versus beam energy for three representative IMF multiplicities. The dashed (dotted) lines in each case indicate the values obtained for spherical (disk-like) particle emission.

expansions or disintegrations. The lower temperature, lower density, and increased surface area of these final, or "freeze-out," configurations afford both increased fragment emission and more similarly sized resultant fragments.[1,2] Thus, the observables N_{IMF} and Z_{IMF} should show a clear sensitivity to such processes. We have calculated the mean values of $\langle N_{IMF} \rangle$ and $\langle Z_{IMF} \rangle$ for all central events, selected via a 10% cut on E_t, and show these values versus the incident beam energy in Figures 2a and 2b.

The solid lines in this figure show the mean values of N_{IMF} and Z_{IMF} calculated for central collisions, while the dotted lines have been added to illustrate two significant points. First, the mean values of these observables exhibit clear and smooth trends with increasing beam energy, following the dotted lines. Second, the values of each of these observables undergo a significant departure from that trend at 65 AMeV, following the solid lines. In the Z_{IMF} case, the enhancement of $\langle Z_{IMF} \rangle$ is already becoming evident at 60 AMeV. These figures thus reveal that not only is there an enhancement in IMF production, but there is also more of the system resulting as IMFs. If the mean values of Z_{IMF} had not shown such an increase at 65 AMeV, the observation would imply that the same portion of the system were simply being broken into smaller pieces; but this is clearly not the case. This observation of enhanced IMF emission and a larger portion of the system resulting as IMFs is again in clear agreement with the theoretical predictions of the formation of non-compact geometries.[1,2]

The fourth and final signature we present is the slope of the ordered charge distribution. To explain, we first order the charges of the detected fragments in each event from largest to smallest, and then calculate a mean value for the first-, second-, $\cdots$, and n^{th}- largest charges. If the charges of these fragments were completely random, the mean values for these ordered charges ($\langle Z_{ord,n} \rangle$) would smoothly

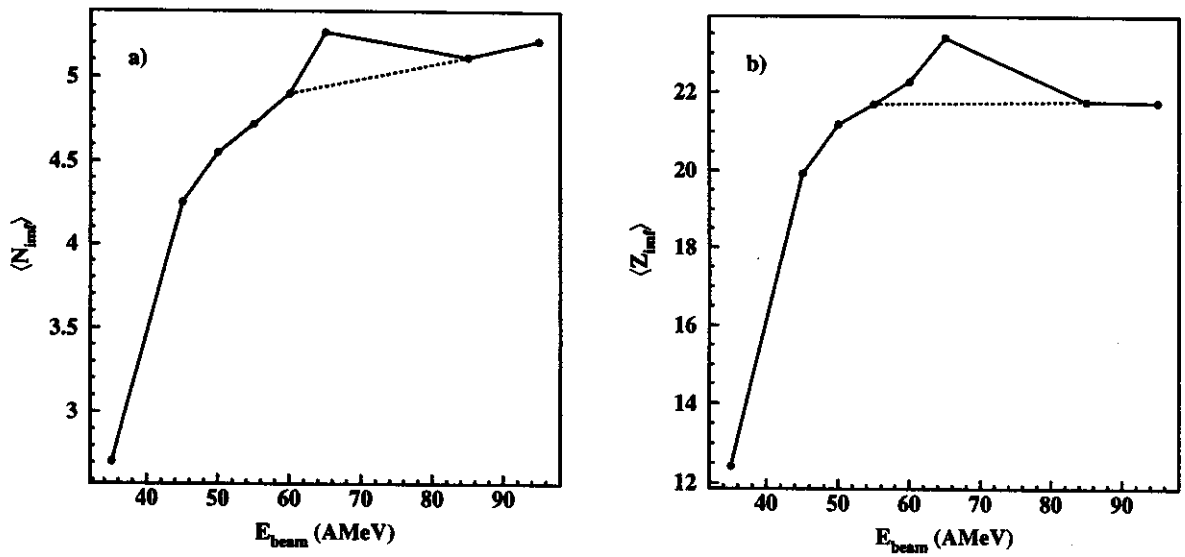

Figure 2: a) $\langle N_{IMF} \rangle$ and b) $\langle Z_{IMF} \rangle$ plotted versus the incident beam energy. The solid lines follow the mean values calculated from the experimental data, while the dashed lines have been added to guide the eye (see text).

decrease with increasing index (n). A straight line fit to such a distribution would have some finite slope value. However, if the charges of these fragments were all the same, the mean values for these ordered charges would also be the same. A straight line fit to this flat distribution would have a zero slope value. Thus, the smaller the slope value of this distribution, the more similar the charges in those events, and so also the converse.

We have calculated the value of this observable for central events, selected via 10% cuts on E_t. We have empirically observed that a power-law (*i.e.* $y(x) \propto x^{-\tau}$) is a better fit function for this distribution than a straight line, so we have extracted the exponent "τ" for central events in all beam energies. The resulting values are plotted in Figure 3 versus the beam energy. The same convention of solid and dotted lines, described above, has been used to illustrate both the overall smooth trend of this observable with increasing beam energy, and the significant departure from that trend manifest in the 65 AMeV case. Once again, this significant suppression in the slope value indicates more equally sized IMFs, which supports the predictions of the formation of non-compact geometries.[3]

3. CONCLUSIONS

We have examined several of these observables, and have found affirmative signatures for the occurrence of non-compact geometries. Our examination of central collisions in the ^{86}Kr+^{93}Nb system reveals the following four clear signatures: 1) a suppression in the mean value of the sphericity of intermediate-mass fragments (IMFs), at an incident beam energy of 60 AMeV; 2) an enhancement in the multiplicity of detected IMFs, at a beam energy of 65 AMeV; 3) an enhancement in the total charge of detected IMFs, at 65 AMeV; and 4) a suppression in the slope of the ordered charge distribution, at 65 AMeV.

We have defined these signatures and their association with the formation of non-compact geometries in this article and, on the basis of this experimental evidence, conclude that non-compact geometries, *e.g.* toroids, are being formed in central collisions for the ^{86}Kr+^{93}Nb system near an incident

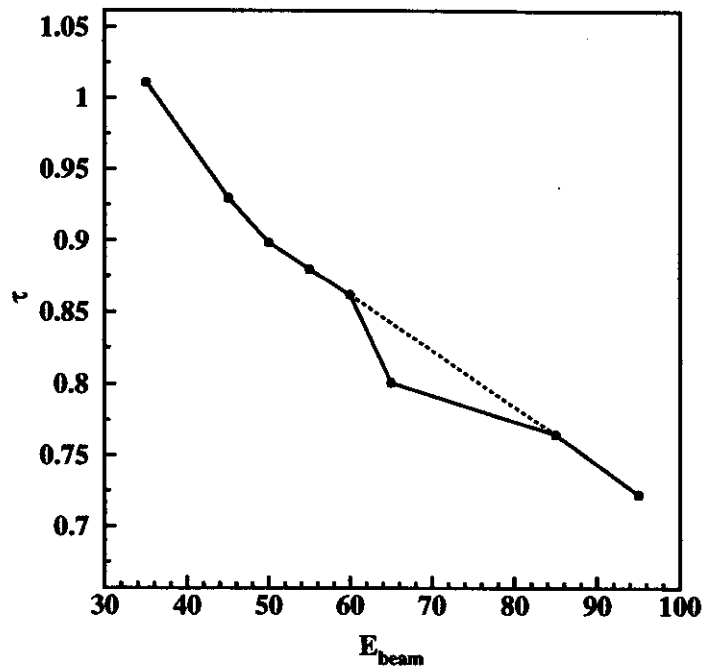

Figure 3: τ versus beam energy, using the same line conventions previously described.

beam energy of 60-65 AMeV. We have not, however, attempted to differentiate which of these geometries is being formed in this article, although the suppression in the sphericity would indicate that it is non-spherical, thus ruling out bubble formation.

a. State University of New York – Stony Brook
b. T.W. Bonner Laboratory, Rice University

References

1. W. Bauer, G.F. Bertsch, and H. Schulz, Phys. Rev. Lett. 69, 1888 (1992).
2. L.G. Moretto, K.Tso, N. Colonna, and G.J. Wozniak, Phys. Rev. Lett. 69, 1884 (1992).
3. H.M. Xu, *et al.*, Phys. Rev. C48, 933 (1993).
4. D.H.E. Gross, B.A. Li, and A.R. DeAngelis, Ann. Phys. (N.Y.) 1, 467 (1992).
5. S.R. Souza and C.Ngô, Phys. Rev. C48, R2555 (1993).
6. A. Guarnera, B. Jacquot, P. Chomaz, and M. Colonna, GANIL Preprint P95-05 (1995).
7. L. Phair, W. Bauer, and C.K. Gelbke, Phys. Lett. B314, 271 (1993).
8. T. Glasmacher, C. Gelbke, and S. Pratt, Phys. Lett. B314, 265 (1993).
9. D. Durand, *et al.*, LPC CAEN Preprint LPCC96-02, Submitted to Phys. Lett. (1996).
10. G.D. Westfall, *et al.*, Nucl. Inst. Meth. A238, 347 (1985).
11. C. Cavata, *et al.*, Phys. Rev. C42, 1760 (1990).
12. J. Cugnon and D. L'Hote, Nucl. Phys. A397, 519 (1983).
13. E.E. Gualtieri, Ph.D. Dissertation, Michigan State University, 1995 (Unpublished).

PARAMETRIZATION OF THE MEMORY EFFECT AT INTERMEDIATE ENERGY

R. Pfaff, D.J. Morrissey, W. Benenson, M. Fauerbach, M. Hellström, C.F. Powell, M. Steiner, B.M. Sherrill, and J.A. Winger[a]

To gain further insight into the influence of the projectile N/Z ratio on the fragment charge dispersion distribution for reactions in the intermediate energy/intermediate mass regime, an experiment was performed using a 75 MeV/nucleon ^{78}Kr beam (~ 45 ppA) impinging on a 102 mg/cm^2 ^{58}Ni target in the medium acceptance target position of the A1200. The main objective of the experiment was to explore the stability of several nuclei important to the rapid proton capture process. The details of the experiment can be found in Ref. [1], along with the binding energy limitations placed on key nuclei. The data obtained during the experiment has now been compared to the results of previous experiments involving fragmentation of neutron-rich krypton projectiles (^{86}Kr and ^{84}Kr [2,3]) in the same energy regime, thus spanning a wide projectile N/Z ratio.

In order to properly include this effect into a semi-empirical fragmentation product cross section code, Sümmerer *et al.* [4] developed a parametrization that took into account previous observations from (target) fragmentation experiments: (i) the maxima of fragment charge distributions always lie on the neutron-deficient side of the valley of β stability, (ii) for targets/projectiles close to β-stability, the most probable charge of a fragment isobaric chain is only dependent on fragment mass, and (iii) the size of the memory effect is different for neutron- and proton-rich projectiles. Chu et al. [5] had described this effect earlier with the equation

$$Z_p(A) = Z_\beta(A) + \Delta \tag{1}$$

where $Z_p(A)$ is the most probable charge and the β-stable charge $Z_\beta(A)$ can be approximated by the smooth function (thus avoiding shell effects) [6]

$$Z_\beta(A) = \frac{A}{1.98 + 0.0155 \cdot A^{2/3}} \tag{2}$$

The Δ term, which describes the difference between experimentally obtained values of Z_p and Z_β, was parameterized by Sümmerer et al. [4] using the form

$$\Delta = \begin{cases} 2.041\text{x}10^{-4} \cdot A^2 & \text{if } A < 66 \\ 2.703\text{x}10^{-2} \cdot A - 0.895 & \text{if } A \geq 66 \end{cases} \tag{3}$$

To describe the additional shift in the charge distribution maxima (Z_p) that is caused by the N/Z ratio of the target/projectile (depending on whether target- or projectile-like residues are studied) an extra "memory effect" term Δ_m was added:

$$Z_p(A) = Z_\beta(A) + \Delta + \Delta_m. \tag{4}$$

A fit to the (scarce) experimental data available at the time led to a parametrization for Δ_m in the form

$$\Delta_m(A) = \left[c_1 \left(\frac{A}{A_t} \right)^2 + c_2 \left(\frac{A}{A_t} \right)^4 \right] \Delta_\beta(A_t) \tag{5}$$

where A_t is the target mass and $\Delta_\beta(A_t) = Z_t - Z_\beta(A_t)$, in which Z_t is the target proton number and A_t is the target mass. Different values for the coefficients c_1 and c_2 were determined for neutron- and proton-rich fragmentation as the memory effect appeared to be smaller for the fragmentation of proton-rich targets/projectiles compared to neutron-rich systems. Figure 1 illustrates the dependence of the memory effect Δ_m on the ratio of A/A_p (where A is the fragment mass and A_p is the projectile mass) for the most abundantly produced final fragment of each isobaric chain (the so-called "ridge line") from the present experiment. The ridge lines are shown also from two other experiments with more neutron-rich krypton isotopes: ^{86}Kr fragmentation at 70 MeV/nucleon [2] and ^{84}Kr fragmentation at 200 MeV/nucleon [3]. Also indicated in Figure 1 by the dashed curve are the results of the parametrization of Eq. 5 for the ^{78}Kr fragmentation (the curves for the reactions involving ^{84}Kr and ^{86}Kr are not shown on the plot, but exhibit similar agreement to the data as that for the ^{78}Kr fragmentation data). It is apparent that the memory effect for intermediate energy/intermediate mass fragmentation behaves differently than expected from the high energy data. Both the data from the current proton-rich fragmentation of ^{78}Kr as well as the data from the neutron-rich fragmentation of ^{84}Kr and ^{86}Kr show a much steeper dependence on the mass ratio than the parametrization. Recent measurements with ^{129}Xe and ^{136}Xe beams at 790 MeV/nucleon showed a similar trend for the proton-rich projectile and the reaction products from the neutron-rich projectile (^{136}Xe) as they deviated from the standard

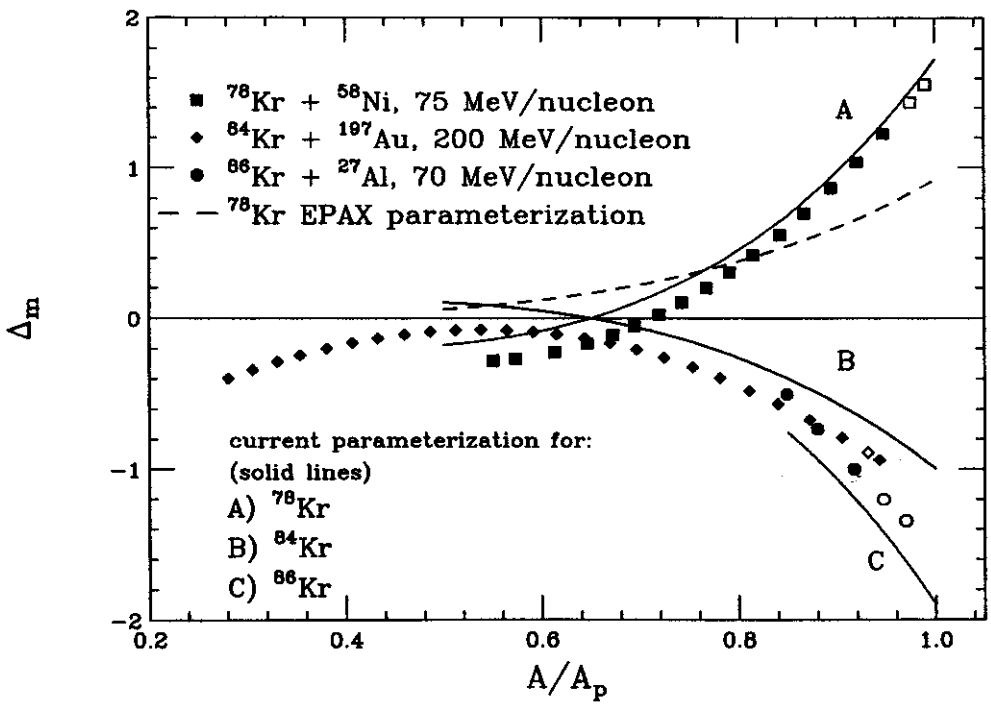

Figure 1: Parametrization of the "memory" effect: the additional shift Δ_m, of the charge-dispersion curve is shown as a function of the fragment to projectile mass ratio. Positive values of Δ_m indicate a shift towards lower N/Z ratios (proton-rich). The isotopic ridge lines from the present experimental data and two previous experiments involving krypton fragmentation [2,3] are shown in the figure. The open symbols indicate charge pick-up products (Z > 36). The dashed curve indicates the parametrization of Sümmerer *et al.* [4] for the ^{78}Kr fragmentation (although not shown, the EPAX parametrization for the ^{84}Kr and ^{86}Kr fragmentation exhibit a similar trend relative to the respective data), while the solid curves represent the modified parametrization derived from the experimental krypton as discussed in text.

parametrization [7]. Using the same formalism as Sümmerer *et al.* [4], the memory effect from the three intermediate-energy krypton fragmentation experiments can best be described by

$$\Delta_m(A) = \left[c_1 \left(\frac{A}{A_t} \right)^4 + c_2 \left(\frac{A}{A_t} \right) \right] \Delta_\beta(A_t) \tag{6}$$

with values of $c_1 = 1.55$ and $c_2 = -0.425$. The modified parametrization was determined by performing a least square fit (with two n-th order polynomial terms) to the experimental data. The c_2 becomes negative to account for the fact that the proton-rich fragmentation data dips below the $\Delta_m = 0$ line (this effect was also observed in the limited data used by Sümmerer *et al.* [4]). The parametrization shows that fragments far from the projectile approach the valley of β stability ($\Delta_m/\Delta_\beta(A_t) \sim 0$) and those near the projectile mass are close to the N/Z ratio of the projectile ($\Delta_m/\Delta_\beta(A_t) \sim 1$). This modified parametrization does a good job reproducing the experimental data as is indicated by solid curves in Figure 1. (Because the ^{86}Kr fragmentation experiment [2] was concentrated on fragments near the Z of the beam, this data is limited to $Z \geq 33$.) It should also be noted that, in contrast to the two other data sets which were measured around 0°, the ^{84}Kr [3] data was obtained at angles of 0.6° and 1.5°. The fact that the ^{84}Kr ridge line in Figure 1 begins to curve downward for $Z < 20$ indicates that parts of the parametrization used in this analysis are not applicable near and below argon ($Z = 18$), as was discussed by Sümmerer *et al.* [4].

Charge pick-up products ($Z > 36$ in this case), which are rarely produced from high energy fragmentation, are commonly observed at intermediate energies. The memory effects for the pick-up products observed in previous krypton fragmentation experiments [2,3], as indicated in Figure 1 by unfilled symbols, seem to closely follow the general trend of the fragmentation products ($Z \leq 36$). This fact, together with the observation that the overall curvature of the memory effect is steeper than the standard parametrization, is a strong indication that the prefragments are produced by processes other than the "pure" fragmentation that occur in high energy reactions. This assumption is also supported by the relatively large pick-up product cross sections that were observed in the current experiment and the ^{86}Kr fragmentation [2].

a. Mississippi State University, Mississippi State, MS 39762, USA

References

1. R. Pfaff *et al.*, 1994 NSCL Annual Report pg. 95.
2. R. Pfaff *et al.*, Phys. Rev. C **51**, 1348 (1995).
3. C. Stéphan *et al.*, Phys. Lett. **262B**, 6 (1991).
4. K. Sümmerer *et al.*, Phys. Rev. C **42**, 2546 (1990).
5. Y.Y. Chu *et al.*, Phys. Rev. C **4**, 2202 (1971).
6. P. Marimer and E. Sheldon, *Physics of Nuclei and Particles* (Academic, New York and London, 1971), Vol. I, p. 15.
7. J. Friese *et al.*, Proc. of the 3rd Int. Conf. on Radioactive Nuclear Beams (East Lansing, USA, May 1993), D.J. Morrissey, Ed., Edition Frontières (Gif-sur-Yvette, France, 1993)., pg. 333.